

# Empirical Constraints on the Nucleosynthesis of Nitrogen

James W. Johnson,<sup>1\*</sup> David H. Weinberg,<sup>1,2,3</sup> Fiorenzo Vincenzo,<sup>1,2</sup> Jonathan C. Bird,<sup>4</sup> and Emily J. Griffith<sup>1</sup>

<sup>1</sup> *Department of Astronomy, The Ohio State University, 140 W. 18th Ave., Columbus, OH, 43210, USA*

<sup>2</sup> *Center for Cosmology and Astroparticle Physics (CCAPP), The Ohio State University, 191 W. Woodruff Ave., Columbus, OH, 43210, USA*

<sup>3</sup> *Institute for Advanced Study, 1 Einstein Dr., Princeton, NJ, 08540, USA*

<sup>4</sup> *Department of Physics & Astronomy, Vanderbilt University, 2301 Vanderbilt Place, Nashville, TN, 37235, USA*

Accepted XXX; Received YYY; in original form ZZZ

## ABSTRACT

We use a multi-ring galactic chemical evolution model to probe the nucleosynthesis of nitrogen (N) in the Milky Way. This approach treats individual annuli in the Galaxy disc as conventional one-zone models, allowing stars to move between rings in a manner based on a hydrodynamical simulation to mimic the effects of stellar migration. We find that in order to reproduce the gas-phase [N/O]-[O/H] relation as observed, N yields must scale roughly linearly with the initial metallicity of the progenitor stellar populations. Of the previously published models for N nucleosynthesis in asymptotic giant branch stars which predict this scaling, their normalization is correct if and only if a substantial fraction of high mass stars collapse directly to black holes rather than exploding as supernovae. Otherwise, we must artificially amplify these N yields to offset the additional oxygen. Our model successfully reproduces many of the observed correlations between stellar N, O, and Fe abundances when their [N/H] measurements are corrected for internal mixing processes known to affect the photospheric compositions of evolved stars. With all of our yield models, N production timescales are sufficiently short such that stellar migration is only a minimal source of intrinsic scatter in the observed gas-phase [N/O]-[O/H] relation. Typical variations in the star formation efficiency produce variations in [N/O] at fixed [O/H] that are a factor of  $\sim 2$  larger than that induced by migration. Our models run using the publicly available *Versatile Integrator for Chemical Evolution* (VICE; <https://pypi.org/project/vice>).

**Key words:** methods: numerical – galaxies: abundances, evolution, star formation, stellar content

## 1 INTRODUCTION

From a nucleosynthesis perspective, nitrogen (N) is a unique element. Along with carbon (C) and helium (He), it is one of only three elements lighter than iron peak nuclei who owe a significant portion of their abundances to asymptotic giant branch (AGB) stars (Johnson 2019). N is also a by-product of the nuclear fusion reactions converting hydrogen (H) into He in stars more massive than the sun with nonzero metallicity. The CNO cycle<sup>1</sup> catalyses the proton-proton chain of nuclear reactions (e.g. Suliga, Shalgar & Fuller 2020) using C, N, and oxygen (O) target nuclei. The slowest component of this chain reaction by far is the  $^{14}\text{N}(\text{p}, \gamma)^{15}\text{O}$  component. As a consequence of this bottleneck, to first order the effect of the CNO cycle is to convert all of the C and O isotopes present in a star's core into  $^{14}\text{N}$ . Furthermore, N is among a select group of elements whose observed abundances in stellar spectra often do not reflect the star's birth abundances. Because N is produced in main sequence stars via the CNO cycle, its abundances in a star's core become enhanced relative to what the star was born with. Upon becoming a red giant, internal mixing processes (i.e. dredge-up) bring this N-enhanced material to the photosphere. This phenomenon is both expected from theoretical

models and observed in open and globular clusters (Gilroy 1989; Korn et al. 2007; Lind et al. 2008; Souto et al. 2018, 2019; Vincenzo et al. 2021).

Both observationally and theoretically, N is among the more well-studied elements. Of particular interest in this paper is the correlation between the abundances of N and O, usually observed in the gas phase. In Fig. 1, we present a compilation of such measurements:

1. HII regions in the first six CHAOS<sup>2</sup> galaxies (NGC 3184, NGC 628, NGC 5194, NGC 5457, M101, NGC 2403; Berg et al. 2020; Skillman et al. 2020; Rogers et al. 2021).
2. HII regions in nearby NGC spirals (Pilyugin, Vílchez & Thuan 2010).
3. HII regions in blue, diffuse star forming dwarf galaxies (Berg et al. 2012; Izotov, Thuan & Guseva 2012; James et al. 2015).
4. Local stars and HII regions (Dopita et al. 2016).
5. Galactic and extragalactic HII regions (Henry, Edmunds & Köppen 2000).
6. Star-forming regions in 550 nearby galaxies in the MaNGA IFU<sup>3</sup> survey (Belfiore et al. 2017).

\* Contact e-mail: [johnson.7419@osu.edu](mailto:johnson.7419@osu.edu)

<sup>1</sup>  $^{12}\text{C}(\text{p}, \gamma)^{13}\text{N}(\beta^+ \nu_e)^{13}\text{C}(\text{p}, \gamma)^{14}\text{N}(\text{p}, \gamma)^{15}\text{O}(\beta^+ \nu_e)^{15}\text{N}(\text{p}, \alpha)^{12}\text{C}$

<sup>2</sup> CHAOS: CHemical Abundances Of Spirals (Berg et al. 2015)

<sup>3</sup> MaNGA: Mapping Nearby Galaxies at Apache Point Observatory (Bundy et al. 2015). IFU: Integral Field Unit.

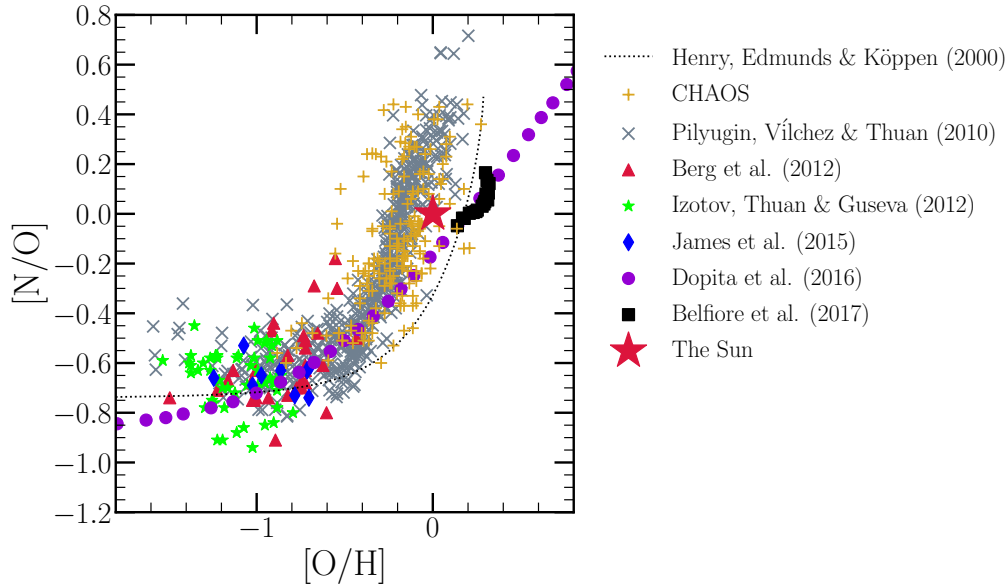


**Figure 1.** The  $[N/O]$ - $[O/H]$  relation as observed in different galactic environments: HII regions from the first six CHAOS galaxies (golden +’s: NGC 3184, NGC 628, NGC 5194, NGC 5457, M101, and NGC 2403; [Berg et al. 2020](#); [Skillman et al. 2020](#); [Rogers et al. 2021](#)) and other nearby NGC spiral galaxies (grey X’s; [Pilyugin et al. 2010](#)), HII regions in blue diffuse star forming dwarf galaxies (red triangles: [Berg et al. 2012](#); green stars: [Izotov et al. 2012](#); blue diamonds: [James et al. 2015](#)), in local stars and HII regions (purple circles: [Dopita et al. 2016](#)), and in the MaNGA IFU survey (black squares: [Belfiore et al. 2017](#)). The fit to  $[N/O]$  as a function of  $[O/H]$  in Galactic and extragalactic HII regions by [Henry et al. \(2000\)](#) is shown in a black dotted line. We omit all uncertainties for visual clarity. The Sun, at (0, 0) on this plot by definition, is marked by a large red star.

Despite intrinsic scatter and some systematic variation in how the abundances are determined, this  $[N/O]$ - $[O/H]$ <sup>4</sup> relation is more or less the same across a wide range of astrophysical environments. Furthermore, recent arguments from both theoretical ([Vincenzo & Kobayashi 2018](#)) and observational perspectives ([Hayden-Pawson et al. 2021](#)) suggest that this relation is largely redshift-invariant. Previous studies have interpreted this universality as an indication that the relation is nucleosynthetic in origin, reflecting the differences between “primary” and “secondary” N production whereby the primary yields do not depend on the initial metal content of a star but the secondary yields do ([Vila-Costas & Edmunds 1993](#); [van Zee, Salzer & Haynes 1998](#); [Henry & Worthey 1999](#); [Pérez-Montero & Contini 2009](#); [Berg et al. 2012](#); [Pilyugin, Grebel & Mattsson 2012](#); [Andrews & Martini 2013](#)). Here we are interested in the origin of both the shape and scatter in this trend using the Milky Way as a case test.

N is not unique in that perhaps the largest source of uncertainty in understanding its abundances is that accurate and precise nucleosynthetic yields from various enrichment channels remain elusive. Presently, no combination of models for nucleosynthesis in and explosions of massive stars is able to reproduce the observed abundance pattern of the elements, and N is no exception ([Griffith et al. 2021a](#)). Recently, [Grisoni, Matteucci & Romano \(2021\)](#) argued that rotating massive stars play a key role in establishing the N abundances seen in metal-poor stars in the Milky Way. Rotation has a considerable impact on the N yields of massive stars, because the internal mixing that it causes ([Zahn 1992](#); [Maeder & Zahn 1998](#); [Lagarde et al. 2012](#)) brings internally produced C and O nuclei into the H-burning shell where they can be processed into <sup>14</sup>N via the CNO cycle ([Heger & Woosley 2010](#); [Frischknecht et al. 2016](#); [Andrews et al. 2017](#)). We

find similar results here comparing various theoretical models for massive star nucleosynthesis (see discussion in § 2.1).

Theoretical models for AGB star nucleosynthesis predict N yields to vary as a function of progenitor mass and metallicity ([Cristallo et al. 2011, 2015](#); [Karakas 2010](#); [Karakas & Lugaro 2016](#); [Karakas et al. 2018](#); [Ventura et al. 2013, 2014, 2018, 2020](#)). In sufficiently massive AGB stars, the base of the convective envelope is hot enough to activate proton capture reactions, allowing the CNO cycle to convert C and O isotopes in <sup>14</sup>N: a process known as hot bottom burning. AGB stars are also known to experience thermal pulsations, and often these pulsations are accompanied by a penetration of the convective envelope into the CO-rich core, bringing some of this material into the envelope: a process known as third dredge-up.<sup>5</sup> When both processes are active, third-dredge up adds new seed nuclei for hot bottom burning to turn into <sup>14</sup>N, substantially increasing the N yields. We demonstrate in §§ 2.2 and 2.3 that various theoretical models predict significantly different N yields for high mass AGB stars as a consequence of how third dredge-up and hot bottom burning occur in the models. The differences in these processes are in turn a consequence of the microphysical assumptions built into the stellar evolution models (e.g. mass loss, opacity, convection and convective boundaries, nuclear reaction networks).

In this paper, we aim to constrain N yields empirically by testing the performance of various “off-the-shelf” yield models within the framework of galactic chemical evolution (GCE) models. To this end we use the multi-zone model for the Milky Way published in [Johnson et al. \(2021\)](#), which treats the Galaxy as a series of concentric rings, describing each ring as a conventional one-zone model of chemical

<sup>5</sup> Here the time adverbial “third” refers only to the fact that these dredge-up episodes are occurring while the star is on the asymptotic giant branch. Because they are associated with the thermal pulsations of AGB stars, there are many episodes of third dredge-up.

<sup>4</sup> We follow standard notation where  $[X/Y] \equiv \log_{10}(X/Y) - \log_{10}(X/Y)_{\odot}$ .

evolution (see discussion in § 3). This approach has been employed in the past to compute abundance simultaneously for many Galactic regions (Matteucci & Francois 1989; Wyse & Silk 1989; Prantzos & Aubert 1995; Schönrich & Binney 2009; Minchev, Chiappini & Martig 2013, 2014; Minchev et al. 2017; Sharma, Hayden & Bland-Hawthorn 2021). In this paper, we assess what is required of N yields in order to reproduce various observed results, in particular the [N/O]-[O/H] relation illustrated in Fig. 1.

By additionally making use of stellar abundance data, we can test the N abundances predicted by our model against observables not available for the gas-phase. Using data from the Apache Point Observatory Galaxy Evolution Experiment (APOGEE; Majewski et al. 2017), Vincenzo et al. (2021) demonstrate that when stellar N abundances are corrected for internal mixing processes, the correlations with stellar age and other elemental abundances are affected. Whether or not our GCE model is able to reproduce their corrected data constitutes a valuable test not only of our understanding of N nucleosynthesis, but also the accuracy of the Vincenzo et al. (2021) measurements which take a model-dependent approach to estimate the birth abundances of N for APOGEE disc stars with available age measurements.

In a sample of 6,507 galaxies from the MaNGA IFU survey (Bundy et al. 2015), Schaefer et al. (2020) demonstrate that the intrinsic scatter in the [N/O]-[O/H] relation at fixed galaxy mass is correlated with variations in the local star formation efficiency (SFE). In regions of slower star formation, [N/O] tends to be slightly higher at fixed [O/H] (see their Fig. 4). This is expected from simple GCE models, because more AGB stars enrich the ISM with N by the time a given [O/H] is reached (e.g. Mollá et al. 2006; Vincenzo et al. 2016a). However, Schaefer et al. (2020) did not rule out stellar migration as an additional source of scatter in the gas-phase [N/O]-[O/H] relation. In principle, there could be a deficit or surplus of N-producing AGB stars in a given Galactic region at any time simply because the orbits are evolving, driving additional scatter in the correlation. The Johnson et al. (2021) GCE model is the ideal tool with which to test this hypothesis. The novel difference between theirs and previous models with similar motivations is that it allows stellar populations to enrich distributions of radii as they migrate. Originally developed to study the abundances of O and iron (Fe), this aspect of Galactic evolution turned out to have an important impact on the delayed type Ia supernova (SN Ia) enrichment of Fe, causing complex fluctuations in the enrichment rates with time at fixed radius. Here we use the same methodology to test for similar effects in the delayed AGB star production of N and to assess the extent to which migration and variability in the SFE drive scatter in the observed [N/O]-[O/H] relation.

## 2 NUCLEOSYNTHESIS

In this paper we make use of the chemical evolution model for the Milky Way presented in Johnson et al. (2021). This model runs using the publicly available Versatile Integrator for Chemical Evolution (VICE; Johnson & Weinberg 2020; Griffith et al. 2021a; Johnson et al. 2021), an open-source PYTHON package designed for GCE modeling. Johnson et al. (2021) focus their discussion of the model predictions on O and Fe, and we retain their yields of these elements here. As required by VICE, the SN yields are defined as the net mass of some element X produced over all explosion events in units of the progenitor cluster’s mass. For example, with a yield of  $y_X = 0.001$ , a hypothetical 1000  $M_\odot$  star cluster would produce 1  $M_\odot$  of the element X instantaneously in the case of core collapse supernovae (CCSNe) or over the delay-time distri-

bution (DTD) in the case of SNe Ia. These yields are net yields in that they do not quantify the metal mass ejected to the interstellar medium (ISM) that was initially present within a star; in the previous example, the 1  $M_\odot$  yield is all newly produced nuclei. We adopt the following values from Johnson et al. (2021), who in turn base them off of Weinberg, Andrews & Freudenberg (2017) and Johnson & Weinberg (2020):

- $y_O^{CC} = 0.015$
- $y_{Fe}^{CC} = 0.0012$
- $y_O^{Ia} = 0$
- $y_{Fe}^{Ia} = 0.00214$ ,

where the subscripts and superscripts differentiate between the element and the SN type. We also assume that N is not produced in significant amounts by SNe Ia (Johnson 2019), and set  $y_N^{Ia} = 0$  throughout this paper accordingly. We spend the remainder of this section detailing our CCSN and AGB star yields of N.

### 2.1 Core Collapse Supernovae and Massive Star Winds

In VICE, CCSN nucleosynthetic products are approximated to be produced instantaneously following an episode of star formation; this is a valid approximation due to how short the lives of massive stars are compared to the relevant timescales for GCE. Based on this and its definition as being in units of a stellar population’s total mass, the yield is simply the constant of proportionality between the CCSN production rate and the star formation rate (SFR):

$$\dot{M}_X^{CC} = y_X^{CC} \dot{M}_\star \quad (1)$$

More generally,  $y_X^{CC}$  quantifies *all* of the nucleosynthetic material approximated to be produced instantaneously following a single stellar population’s formation, though the majority of such events should be associated with massive stars or their SNe. In the case of N specifically, a substantial amount emerges in winds before the actual SN itself, allowing massive stars to produce a lot N even if they collapse directly to a black hole (Griffith et al. 2021a).

We compute theoretically predicted values of  $y_N^{CC}$  using VICE’s `vice.yields.ccsne.fractional` function assuming a Kroupa (2001) IMF; details on how VICE handles these calculations can be found in § 4 of Griffith et al. (2021a) and in the VICE science documentation<sup>1</sup>. In the left panel of Fig. 2, we plot the results as a function of progenitor metallicity as predicted by the Woosley & Weaver (1995), Nomoto, Kobayashi & Tominaga (2013), Sukhbold et al. (2016), and Limongi & Chieffi (2018) tables. There is good agreement between the various non-rotating models, but only Limongi & Chieffi (2018) report yields for progenitors with non-zero rotational velocities; these yields are substantially larger than that of their non-rotating counterparts. Most of the N production in CCSN progenitors occurs via the CNO cycle processing C and O isotopes into  $^{14}\text{N}$ , and with few C and O seed nuclei at low  $Z$ , production of  $^{14}\text{N}$  is difficult. Rotation-induced mixing, a highly uncertain process (Zahn 1992; Maeder & Zahn 1998; Lagarde et al. 2012), could transport newly produced C and O into the hydrogen burning shell of the CCSN progenitor, facilitating  $^{14}\text{N}$  production (Frischknecht et al. 2016; see also discussion in § 4.2 of Andrews et al. 2017). For this reason, N yields at low metallicity are quite sensitive to these assumptions about stellar rotation and internal mixing

<sup>1</sup> [https://vice-astro.readthedocs.io/en/latest/science\\_documentation/yields](https://vice-astro.readthedocs.io/en/latest/science_documentation/yields)

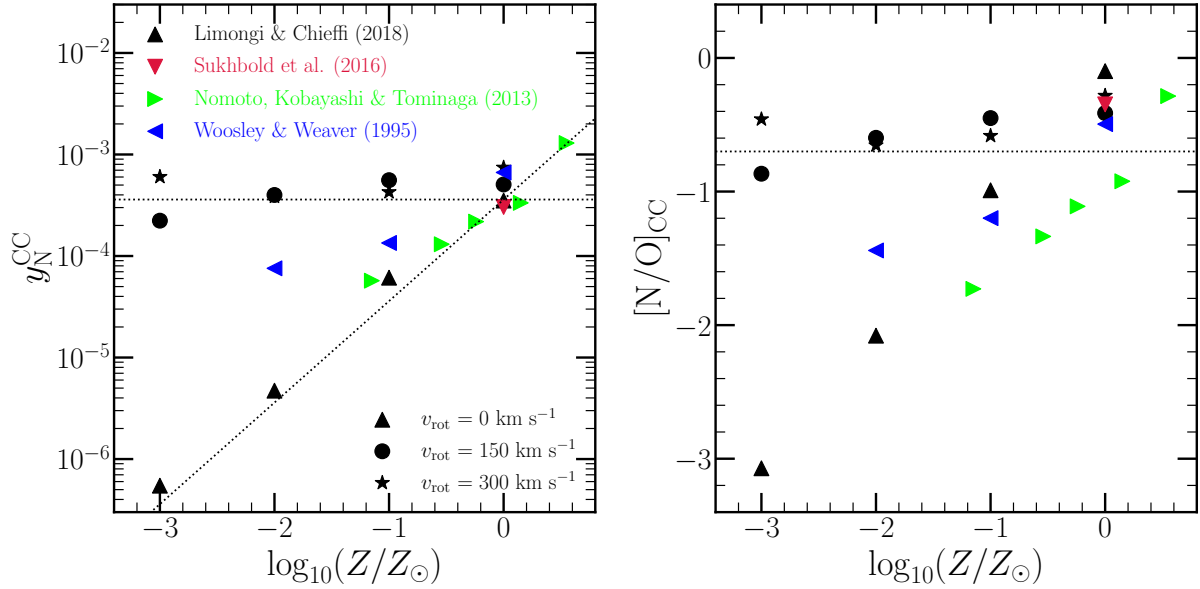


**Figure 2.** **Left:** IMF-averaged CCSN yields of N calculated using VICE’s `vice.yields.ccsne.fractional` function with the tables published by Woosley & Weaver (1995, blue), Nomoto et al. (2013, green), Sukhbold et al. (2016, red), and Limongi & Chieffi (2018, black). All studies report yields for non-rotating progenitors, shown by the triangles; for visual clarity, the triangles point in a different direction for each study according to the legend. Limongi & Chieffi (2018) report additional yields for progenitors with rotational velocities of 150 (circles) and 300 km/s (stars). The horizontal dashed line marks  $y_N^{\text{CC}} = 3.6 \times 10^{-4}$ , the value of our fiducial CCSN yield of N in our GCE models. We use the form shown by the slanted line (equation X) in § X in combination with some of our AGB star yield models discussed in § 2.2. **Right:** The  $[N/O]$  ratio predicted by each of the explosion models in the left-hand panel, under the same colour-coding and marker scheme. We mark the position of  $[N/O] = -0.7$  with a black dotted line, the value roughly suggested by the observations of low-metallicity systems highlighted in Fig. 1.

processes (Heger & Woosley 2010), and consequently IMF-averaged yields are highly uncertain.

Based on the definition of the abundance ratio  $[X/Y]$ , we can compute the  $[N/O]$  ratio of CCSN ejecta from the values of  $y_N^{\text{CC}}$  and  $y_O^{\text{CC}}$  predicted from a given yield table:

$$[N/O]_{\text{cc}} = \log_{10} \left( \frac{y_N^{\text{CC}}}{y_O^{\text{CC}}} \right) - \log_{10} \left( \frac{Z_{N,\odot}}{Z_{O,\odot}} \right), \quad (2)$$

where  $Z_{X,\odot}$  is the abundance by mass of some element X in the sun, for which we take  $Z_{N,\odot} = 6.91 \times 10^{-4}$  and  $Z_{O,\odot} = 5.72 \times 10^{-3}$  based on the solar photospheric abundances of Asplund et al. (2009). For each of the published yield tables and rotational velocities in the left panel of Fig. 2, we compute the corresponding values of  $y_O^{\text{CC}}$  using VICE and plot the resultant values of  $[N/O]_{\text{cc}}$  in the right panel. These yield ratios follow similar trends with progenitor metallicity and rotation as  $y_N^{\text{CC}}$  itself, a consequence of the fact that these studies predict relatively metallicity-independent O yields.

CCSN yields can to some extent be empirically calibrated by ensuring that they reproduce the  $[N/O]$  ratios of low metallicity systems. Since AGB star yields of N are believed to depend on the progenitor’s metallicity (see discussion in § 2.2 and references therein), it’s likely that the “plateau” in  $[N/O]$  at low  $[O/H]$  reflects the IMF-averaged CCSN yields of N and O. Fig. 1 suggests that  $[N/O]_{\text{cc}} = -0.7$ ; we highlight this value in the right panel of Fig. 2 with a horizontal black dashed line. Given this observational result and our adopted value of  $y_O^{\text{CC}} = 0.015$ , we compute that an empirical N yield of  $y_N^{\text{CC}} = 3.6 \times 10^{-4}$  using equation (2). We adopt this value as our fiducial CCSN yield of N and highlight it with a horizontal black dashed line in the left panel of Fig. 2. We discuss the sloped dotted

line in that panel in the context of some of our AGB star yield models in § X.

These empirical values of  $[N/O]_{\text{cc}}$  and  $y_N^{\text{CC}}$  are in good agreement with the rotating CCSN models of Limongi & Chieffi (2018). This supports the recent argument by Grisoni et al. (2021) that rotating massive stars play an important role in establishing the N abundances observed at low metallicities in the Milky Way. Although the Sukhbold et al. (2016) tables agree nearly perfectly with our empirical value of  $y_N^{\text{CC}} = 3.6 \times 10^{-4}$ , they overestimate  $[N/O]_{\text{cc}}$  by  $\sim 0.2$  dex; this is because they predict a value of  $y_O^{\text{CC}}$  lower than our adopted value of 0.015. Although most of the supernova models plotted in Fig. 2 slightly overestimate our empirical value of  $[N/O]_{\text{cc}} = -0.7$ , they still fall short of solar. This implies the need for an additional enrichment, which is expected because it is well understood that N is also produced in considerable amounts by AGB stars (Johnson 2019).

## 2.2 Asymptotic Giant Branch Stars

Similar to our SN yields (see discussion in § 2.1), our AGB star yields are fractional net yields in that they quantify only the newly produced mass of an element X in units of the progenitor star’s zero-age main sequence (ZAMS) mass. For a yield  $y_X^{\text{AGB}}(M_{\star}, Z_{\star})$ , the mass yield is then given by  $M_{\star} y_X^{\text{AGB}}(M_{\star}, Z_{\star})$ . AGB star enrichment proceeds as it does in Johnson & Weinberg (2020) under the caveat that the yield is placed in the  $\delta R_{\text{gal}} = 100$  pc ring that a stellar population is in at a given time. In short, VICE implements an algorithm which computes the mass in dying stars from each stellar population, and the ZAMS mass required to compute the fractional yield comes from a mass-lifetime relationship; for the latter, we adopt the parabola



in  $\log \tau - \log m$  space from [Larson \(1974\)](#) (see discussion of the mass-lifetime relationship in VICE in Appendix A).

Here we make use of four previously published tables of AGB star yields calculated from stellar evolution models, each of which are sampled on a grid of progenitor masses and metallicities. To approximate  $y_X^{\text{AGB}}$  as a smooth function of  $M_\star$  and  $Z_\star$ , VICE interpolates bi-linearly between grid elements - once in mass and once in metallicity - and linearly extrapolates above or below in either quantity as necessary. By comparing the predicted N abundances of the [Johnson et al. \(2021\)](#) chemical evolution model for the Milky Way to the latest observational data, we can constrain how accurately these “off-the-shelf” yield models characterize how and where N is produced:

1. [Karakas \(2010, hereafter K10\)](#)<sup>2</sup> published yields for  $Z = 0.0001, 0.004, 0.008$ , and  $0.02$  progenitors. We plot these yields in the upper left panel of Fig. 3.
2. [Karakas & Lugaro \(2016\)](#) and [Karakas et al. \(2018\)](#) published yields for  $Z = 0.0028, 0.007, 0.014$ , and  $0.03$  progenitors; we hereafter refer to these yields as the **KL16+K18** model. We plot a subset of these yields in the upper middle panel of Fig. 3.
3. We combine the yields for  $Z = 0.0003$  and  $0.008$  progenitors from [Ventura et al. \(2013\)](#) with those at  $Z = 0.004$  from [Ventura et al. \(2014\)](#), at  $Z = 0.014$  from [Ventura et al. \(2018\)](#), and at  $Z = 0.04$  from [Ventura et al. \(2020\)](#) into a single table of yields. In this set, we also include a set of un-published yields at  $Z = 0.001$  and  $0.002$  computed with similar stellar models (provided by P. Ventura, private communication). We hereafter refer to this yield set as the **V13** model, and we illustrate a subsample of these yields in the upper right panel of Fig. 3.
4. [Cristallo et al. \(2011, 2015\)](#) published yields for  $Z = 0.0001, 0.0003, 0.001, 0.002, 0.003, 0.006, 0.008, 0.01, 0.014$ , and  $0.02$  progenitors; we hereafter refer to these yields as the **C11+C15** model. This is the default set of yields in VICE. It is also the software’s most comprehensive set of previously published AGB star yields in that it includes tables for all elements built into the code and is sampled at the most metallicities. We illustrate a subsample of these yields in the lower left panel of Fig. 3.

VICE also allows users to construct their own functions of progenitor mass and metallicity to describe the AGB star yield. Motivated by the roughly linear of the **C11+C15** yields and their general success in our fiducial model once renormalized by a constant factor (see discussion in § 4), we construct a model in which the yield is linearly proportional to both progenitor ZAMS mass and metallicity:

$$y_N^{\text{AGB}} = \xi \left( \frac{M}{M_\odot} \right) \left( \frac{Z}{Z_\odot} \right) \quad (3)$$

We illustrate this model in the lower middle panel of Fig. 3 for  $\xi = 3 \times 10^{-4}$  in comparison to the **C11+C15** yields shown by the coloured X’s.

Despite reporting values of the same physical quantities, the N yields reported by each of these studies show substantial differences between one another. Unfortunately, ascertaining the origins of these differences is difficult because each study employs different assumptions for important evolutionary parameters such as opacity, mass loss, nuclear reaction networks, and convection and convective boundaries within stars, all of which have a significant impact

on stellar evolution and thus the predicted yields (see discussion in, e.g., § 5 of [Karakas & Lugaro 2016](#)). However, the differences can largely be understood by considering two important phenomena known to occur within AGB stars: third dredge-up (TDU) and hot bottom burning (HBB). Collapsing the information into these two processes is helpful because their differences arise as a consequence of the different input physics between the stellar evolution models.

TDU refers to the repeated penetrations of the convected envelope into the hydrogen-depleted core during the thermal pulses associated with AGB star evolution. This process does not affect N abundances much because at this evolutionary phase, the core is mostly composed of C and O. However, the  $^{13}\text{C}(\alpha, n)^{16}\text{O}$  reaction can occur at substantial rates when the core material is mixed with the He-rich shell during each TDU episode. This reaction is the main source of free neutrons in low mass AGB stars, and as a consequence, each replenishment of C does indirectly contribute to raising an AGB star’s overall yield. HBB refers to proton capture reactions at the base of the convective envelope. This activates the CNO cycle, producing large amounts of  $^{14}\text{N}$  at the expense of C and O isotopes. HBB requires a higher mass AGB star progenitor ( $M_{\text{ZAMS}} = 4 - 5 M_\odot$  at  $Z_\odot$  according to [Karakas 2010](#)) than TDU ( $M_{\text{ZAMS}} = 2 - 2.5 M_\odot$  at  $Z_\odot$  according to [Karakas 2010](#)), but the minimum mass for both decreases at lower metallicities.

The most efficient N production occurs when both TDU and HBB are active within an AGB star, because each replenishment of C and O isotopes by TDU adds new seed nuclei for the CNO cycle when HBB is active. This is the reason for the substantial N production above  $\sim 4 M_\odot$  in the **K10** and **KL16+K18** models; in both yield sets, every star that experiences HBB also experiences TDU (see Table 1 in both [Karakas 2010](#) and [Karakas 2014](#), which describes the stellar evolution models from which the **KL16+K18** yields are computed). Both TDU and HBB are more efficient at low metallicity (see discussion in [Ventura et al. 2013](#)). In the case of TDU, each penetration into the core by the convective envelope is deeper due to the lower opacity. For HBB, the base of the convective is hotter at low  $Z$ , and the rate of CNO cycle reactions is an extremely strong function of temperature. This interaction between TDU and HBB is also the reason for the increase in N yields in the **V13** tables near  $\sim 3 M_\odot$ . Unlike the **K10** and **KL16+K18** models, their stars experience both TDU and HBB only in this narrow mass range.

Of all of these yields taken from the literature, the **C11+C15** sample shows the smoothest dependence on progenitor mass and metallicity. Unfortunately, ascertaining the exact cause of this difference between other yields explored here is difficult even when collapsing the information into TDU and HBB. Relative to the **KL16+K18** yields (see discussion in § 5 of [Karakas & Lugaro 2016](#)), the **C11+C15** models have more mass loss, a  $\sim 10\%$  faster triple- $\alpha$  reaction rate, fewer thermal pulses overall, and weaker HBB due to a lower temperature at the base of the convective envelope. Though their agreement is good below  $\sim 3 M_\odot$ , the fact that HBB is weaker and there are fewer TDU episodes does however lend a qualitative explanation into why the **C11+C15** yields are so much smaller than the **K10** and **KL16+K18** yields at higher masses.

Although both the **K10** and **KL16+K18** yield models both show a substantial increase in N yields above  $\sim 4 M_\odot$ , there are some notable differences between the two. In particular, the yields at solar metallicity are somewhat higher in the newer version. Some of this

<sup>2</sup> We clarify that our abbreviations of these papers (i.e. **K10**, **KL16+K18**, **V13**, and **C11+C15**) refer specifically to their yields of N as we adopt them in our model. We cite the full names of these papers when referring to their more general results.

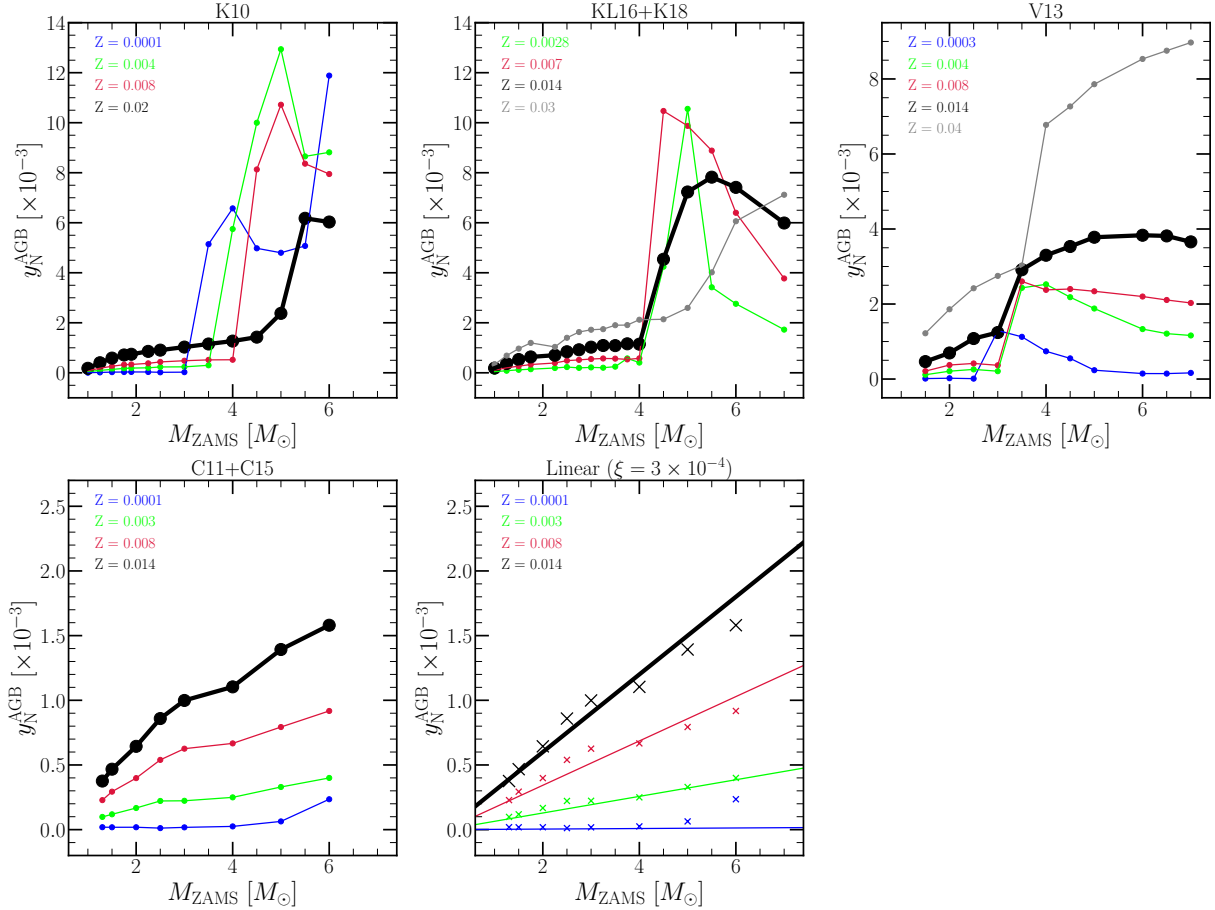


**Figure 3.** The fractional yields of N from AGB stars  $y_N^{\text{AGB}}$  as a function of progenitor ZAMS mass and birth metallicity  $Z$  as reported by Karakas (2010, upper left), Karakas & Lugaro (2016) and Karakas et al. (2018, upper middle), Ventura et al. (2013, 2014, 2018, 2020, upper right), and Cristallo et al. (2011, 2015, lower right). For Ventura et al. (2013, 2014, 2018, 2020) and Cristallo et al. (2011, 2015), we show the yields only for a selection of metallicities available from their provided tables. We highlight yields at solar metallicity ( $Z = 0.02$  for Karakas 2010,  $Z = 0.014$  otherwise) with bold black lines. In the lower right panel, we show the yields predicted by our linear model (coloured lines, see discussion in § 2.2) in comparison to the Cristallo et al. (2011, 2015, coloured X's) predictions.

can be attributed to the now-lowered solar metallicity<sup>3</sup> ( $Z = 0.014$  in KL16+K18 compared to  $Z = 0.02$  in K10) and the effect that has on TDU and HBB, but this does not account for all of the differences. Furthermore, the yields at sub-solar metallicities decreased slightly from K10 to KL16+K18, particularly for the highest mass AGB stars. These differences can be understood by slight variations in the input physics (A. Karakas, private communication). Based on updated opacity tables, the KL16+K18 models are slightly hotter and more compact; consequently, they experience hotter HBB and deeper TDU. Experiencing more thermal pulses overall and consequently a longer AGB lifetime, the KL16+K18 stars have more time for HBB to convert  $^{12}\text{C}$  into  $^{14}\text{N}$ . At lower metallicity, KL16+K18 use low-temperature opacity tables based on Marigo (2002) that more closely follow the surface composition of the star. These opacities are higher, making the stars larger and increasing the mass-loss rate relative to K10. The  $Z = 0.0028$  model from Karakas et al. (2018)

uses the Bloeker (1995) mass-loss prescription as opposed to that of Vassiliadis & Wood (1993) as in both Karakas (2010) and Karakas & Lugaro (2016). This choice results in fewer thermal pulses and a shorter AGB lifetime. Each of these effects at low metallicity act to decrease the overall yield of  $^{14}\text{N}$ .

In the interest of consistency, when we adopt a particular AGB star yield model for N, we also adopt the corresponding table within VICE for O and Fe when possible.<sup>4</sup>

### 2.3 IMF-Averaged AGB Star Yields: Metallicity and Time Dependence

To more directly compare the K10, KL16+K18, V13, and C11+C15 AGB star yield models of N to one another, we plot IMF-weighted yields from each of them at solar metallicity ( $Z = 0.02$  for K10,  $Z = 0.02$  otherwise) in the left hand panel of Fig. 4. As

<sup>3</sup> Changes in the accepted value of the metallicity of the sun trace back to the canonical value of  $\sim 2\%$  derived by Anders & Grevesse (1989), Grevesse & Noels (1993), and Grevesse & Sauval (1998) later being revised to  $\sim 1.4\%$  by Lodders (2003), Asplund, Grevesse & Sauval (2005), Lodders, Palme & Gail (2009), Asplund et al. (2009), and Asplund, Amarsi & Grevesse (2021).

<sup>4</sup> In the case of Ventura et al. (2013, 2014, 2018, 2020), AGB star yields of Fe are not available. In the case of our linear model which applies only to N, we assume the VICE default of the Cristallo et al. (2011, 2015) yields for both O and Fe.

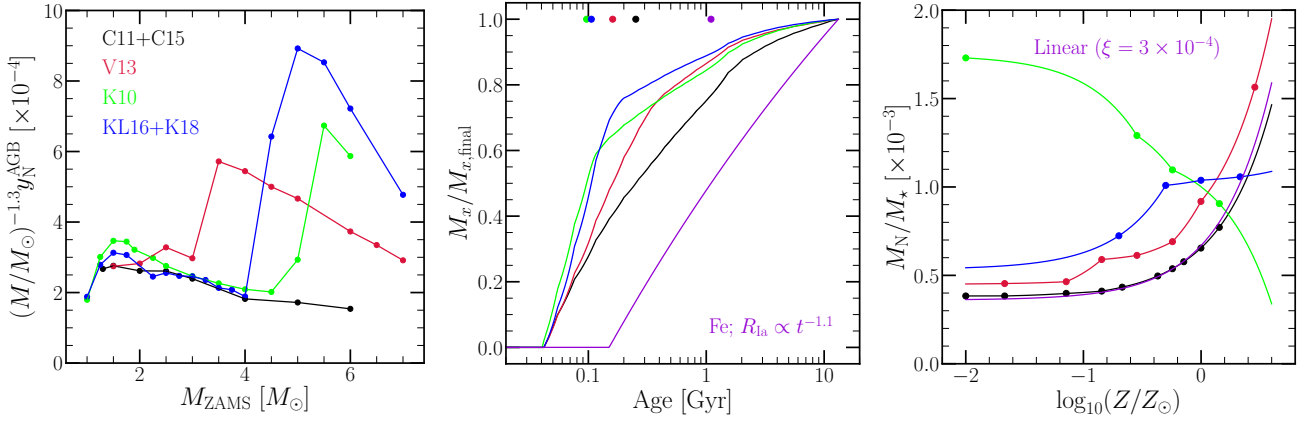


**Figure 4.** **Left:** The IMF-weighted mass yield of N from AGB stars as a function of progenitor ZAMS mass at solar metallicity ( $Z = 0.02$  in K10,  $Z = 0.014$  otherwise). **Middle:** The net mass of N produced by AGB stars from a single stellar population for each of our yield models at solar metallicity. The purple line denotes the same for Fe assuming our  $t^{-1.1}$  DTD as in the Johnson et al. (2021) chemical evolution model. All values are normalized to the total mass produced at an age of 13.2 Gyr. Points at the top of the panel denote the ages at which 50% of the total mass yield has been produced. **Right:** The total amount of N produced by a 13.2 Gyr old stellar population as a function of metallicity for each of our yield models normalized by the stellar population’s initial mass. Points mark metallicities at which the published tables report yields.

mentioned in § 2.2, the AGB star yield of N  $y_N^{\text{AGB}}$  as we have parameterized it is in units of the progenitor star’s ZAMS mass, and consequently the *mass yield* of N is given by  $M_{\star} y_N^{\text{AGB}}$ . With an additional weight of  $M_{\star}^{-2.3}$  from the IMF in this mass range (e.g. Kroupa 2001), we therefore multiply the values of  $y_N^{\text{AGB}}$  by  $(M_{\star}/M_{\odot})^{-1.3}$  to quantify the total mass yield of N taking into account the intrinsic mass distribution of stars. Even with the additional weight of  $M_{\star}^{-1.3}$ , the C11+C15 yields are relatively mass-independent. For other studies, the contributions from higher mass AGB stars is yet more pronounced due to the effects of TDU and HBB discussed in § 2.2.

In the middle panel of Fig. 4, we plot the AGB star production of N from a single stellar population as a function of its age. For this we use VICE’s `vice.single_stellar_population` function which computes the mass yield of a given element as a function of age from a star cluster of known metallicity. For the sake of this calculation, we set all CCSN yields of N to zero in order to highlight the AGB star contribution. We show the results of this procedure for solar metallicity only (again  $Z = 0.02$  for K10,  $Z = 0.014$  otherwise), and we normalize all values to the total mass produced at  $T = 13.2$  Gyr.

Under the C11+C15 yields, it takes  $\sim 250$  Myr for a single stellar population to produce  $\sim 50\%$  of its N from AGB stars, as noted by the coloured points at the top of the panel. This is a rather short characteristic delay time considering that these yields are relatively mass-independent when weighted by the IMF, suggesting instead that most of the N yield under this model is actually coming from higher mass ( $\geq 2 M_{\odot}$ ) AGB stars. This traces back to the steep nature of the stellar mass-lifetime relation (e.g. Larson 1974; Maeder & Meynet 1989; Padovani & Matteucci 1993). Even though the IMF-weighted yields suggest roughly equal contributions per small interval in mass  $dM_{\star}$ , this quantifies the contributions per small interval in age  $d\tau$ . As a stellar population ages, the enrichment rates will inevitably slow down considerably as the mass range  $dM_{\star}$  gets progressively narrower as  $\tau$  increases. As expected due to their larger IMF-weighted contributions to N from high mass AGB stars, our other yield models predict even shorter characteristic delay times.

For comparison, we plot the enrichment of Fe by our  $t^{-1.1}$  power-law DTD, also with the CCSN yield set to zero to highlight the SN Ia contribution. The characteristic delay time for Fe production is

longer than that of N by nearly an order of magnitude - exactly how much depending on which AGB star yield model is selected. As noted in Johnson et al. (2021), a delay-time of  $\sim 1$  Gyr is exactly as expected for a  $\sim t^{-1}$  DTD because half of the SNe Ia occur between 100 Myr and 1 Gyr and the other half between 1 Gyr and 10 Gyr.

In the right panel of Fig. 4, we plot the total amount of N produced by a 13.2 Gyr old single stellar population as a function of its metallicity according to all of our AGB star yield models, including the linear model (see discussion in § 2.2). For this calculation, we retain our CCSN yield of N (see discussion in § 2.1):  $y_N^{\text{CC}} = 3.6 \times 10^{-4}$ . In general, there is good qualitative agreement between the C11+C15 and the V13 models, the only major difference being the normalization. The predictions with the linear model with  $\xi = 3 \times 10^{-4}$  are nearly identical to the C11+C15 model, though this is unsurprising given their similarity in Fig. 3. The value at which these N yields flatten off at low  $Z$  is reflective of our adopted value of  $y_N^{\text{CC}}$ . Up to  $\log_{10}(Z/Z_{\odot}) \approx -0.2$ , the KL16+K18 yields predict a similar trend as C11+C15 and V13, also with a difference in normalization, but at solar and super-solar metallicities they predict much more metallicity-independent N yields than others. The K10 yields, on the other hand, do not agree with any of the other models, instead predicting N yields to *decrease* monotonically with increasing  $Z$ . These differences between the K10 and KL16+K18 models traces back to differences regarding the opacity and mass loss prescriptions between these two models (see discussion in § 2.2). We demonstrate in § 4.2 that N yields which scale roughly linearly with metallicity as in the C11+C15 and V13 models are required in order to reproduce the [N/O]-[O/H] relation as observed. The normalization, however, depends on the SN yields.

### 3 THE MULTI-ZONE CHEMICAL EVOLUTION MODEL

We use the fiducial chemical evolution model for the Milky Way published in Johnson et al. (2021), which runs using the VICE chemical evolution code (Johnson & Weinberg 2020; Griffith et al. 2021a; see Appendix A). Johnson et al. (2021) focus their discussion on the predicted O and Fe abundances, but because VICE recognizes most elements on the periodic table, computing N abundances with this

model is easy. Multi-zone models allow simultaneous calculations of enrichment rates and abundances for multiple Galactic regions, making them a more appealing option than classical one-zone models for a system like the Milky Way. Furthermore, they can take into account stellar migration in a framework that is much less computationally expensive than hydrodynamical simulations, making them the ideal experiments for our purposes. We provide a brief summary of the model here, but a full breakdown can be found in § 2 of [Johnson et al. \(2021\)](#).

As in previous models for the Milky Way (e.g. [Matteucci & Francois 1989](#); [Schönrich & Binney 2009](#); [Minchev et al. 2013, 2014, 2017](#); [Sharma et al. 2021](#)), this model parameterizes the Galaxy disc as a series of concentric rings of uniform width  $\delta R_{\text{gal}} = 100$  pc. Each ring is assigned its own star formation history (SFH), and with assumptions about the  $\Sigma_{\text{gas}} - \dot{\Sigma}_{\star}$  and outflows (see discussion below), VICE computes the implied amounts of gas and infall at each timestep automatically. Under the caveat that stellar populations can move between rings and place their nucleosynthetic products in a ring other than the one they were born in, each ring is otherwise described by a conventional one-zone GCE model. Tracking enrichment as stars migrate was a novel addition by the [Johnson et al. \(2021\)](#) model which they demonstrate to have a significant impact on the enrichment rates from delayed sources such as SNe Ia.

To drive stellar migration, the model makes use of star particles from a hydrodynamical simulation, for which [Johnson et al. \(2021\)](#) select the h277 galaxy from the [Christensen et al. \(2012\)](#) suite evolved with the N-body+SPH code GASOLINE ([Wadsley et al. 2004](#), SPH: Smoothed Particle Hydrodynamics); we retain this decision here. Previous studies have shown that h277, among other disc galaxies evolved with similar physics, has a realistic rotation curve ([Governato et al. 2012](#); [Christensen et al. 2014a,b](#)), stellar mass ([Munshi et al. 2013](#)), metallicity ([Christensen et al. 2016](#)), dwarf satellite population ([Zolotov et al. 2012](#); [Brooks & Zolotov 2014](#)), HI properties ([Brooks et al. 2017](#)), and stellar age-velocity relation ([Bird et al. 2021](#)). Despite this, there are some interesting differences between h277 and the Milky Way. First and foremost, h277 had only a weak and transient bar, lacking one at the present day, while the Milky Way is known to have a strong, long-lived central bar (e.g. [Bovy et al. 2019](#)). This could indicate that the dynamical history of h277 and its star particles differs significantly from that of the Milky Way. Furthermore, the last major merger in h277 was at a redshift of  $z \approx 3$ , making it an interesting case study for its quiescent merger history (e.g. [Zolotov et al. 2012](#)), while the Sagittarius dwarf galaxy, a relatively massive satellite, is believed to have made pericentric passages around the Milky Way at 1–2 Gyr intervals ([Law & Majewski 2010](#)). With this in mind, a dynamical history such as that of h277 in this GCE model can be thought of as capturing purely secular galaxy evolution. Although these differences between h277 and the Milky Way are well understood, their impact on chemical evolution is not. We are unaware of any studies which investigate the impact of different assumptions regarding the Galaxy’s dynamical history and the subsequent effects on predicted abundances; this would be an interesting direction for future work.

Radial migration of stars proceeds from the h277 star particles in a simple manner; for a stellar population in our model born at a radius  $R_{\text{gal}}$  and a time  $T$ , VICE searches for star particles born at  $R_{\text{gal}} \pm 250$  pc and  $T \pm 250$  Myr. From the star particles that make this cut, it then randomly selects one to act as that stellar population’s *analogue*. The stellar population then assumes the present day midplane distance  $z$  and the change in orbital radius  $\Delta R_{\text{gal}}$  of its analogue. In the [Johnson et al. \(2021\)](#) fiducial model, stellar populations move to their implied final radii with a  $\sqrt{\text{age}}$  dependence, similar to

the assumption made by [Frankel et al. \(2018, 2019\)](#). Although they investigate other assumptions for this time-dependence, in the present paper we make use of only this model (hereafter referred to as the “diffusion” model) and an idealized one in which stars remain at their birth radius and then instantaneously migrate at the present day (hereafter referred to as the “post-processing” model). If VICE does not find any star particles from h277 in its initial  $R_{\text{gal}} \pm 250$  pc and  $T \pm 250$  Myr search, it widens it to  $R_{\text{gal}} \pm 500$  pc and  $T \pm 500$  Myr; if still no candidate analogues are found, VICE maintains the  $T \pm 500$  Myr requirement, but assigns the star particle with the smallest difference in birth radius as the analogue. This procedure can be thought of as “injecting” the dynamics of the h277 galaxy into our multi-zone chemical evolution model, and can in principle be repeated for any hydrodynamical simulation of a disc galaxy. As in [Johnson et al. \(2021\)](#), we neglect radial gas flows (e.g. [Lacey & Fall 1985](#); [Bilitewski & Schönrich 2012](#); [Vincenzo & Kobayashi 2020](#)), instead focusing on the impact of stellar migration.

Although this model does impose some small but nonzero level of star formation at early times in the outer disc, the sample of star particles from h277 is sufficiently large such that stellar populations that form there are typically assigned analogues which formed within  $\sim 2$  kpc of their birth radius. While ignoring effects such as the radial growth of the Galaxy (e.g. [Bird, Kazantzidis & Weinberg 2012](#); [Bird et al. 2013](#)), this at least ensures that these old, outer disc populations are assigned star particles which given them an outer disc rather than an inner disc dynamical history.

Rather than using a hydrodynamical simulation, some previous studies have implemented stellar migration using dynamical arguments (e.g. [Schönrich & Binney 2009](#); [Sharma et al. 2021](#)). An advantage of our approach over this is that these dynamical arguments introduce free parameters into the model which then require fitting to data. It is also unclear the extent to which fitting to observed data biases the model into agreement with parts of the sample not involved in the fit. A disadvantage is that we are restricted to one realization of our dynamical history; slight variations are not possible. We do not distinguish between “blurring” and “churning”: terms often used to refer to the epicyclic motions of stars and changes in their guiding centre radii, respectively. These effects are induced by a variety of physical interactions such as molecular cloud scattering ([Mihalas & Binney 1981](#); [Jenkins & Binney 1990](#); [Jenkins 1992](#)), orbital resonances with spiral arms or bars ([Sellwood & Binney 2002](#); [Minchev et al. 2011](#)), and satellite perturbations ([Bird et al. 2012](#)). All of these effects are present in h277 and should therefore be inherited to some extent by the stellar populations in our GCE model.

Our fiducial model here has the same SFH as that of [Johnson et al. \(2021\)](#), where the time-dependence at a given  $R_{\text{gal}}$  is given by

$$\dot{\Sigma}_{\star} \propto (1 - e^{-t/\tau_{\text{rise}}})e^{-t/\tau_{\text{sfr}}}, \quad (4)$$

where  $\tau_{\text{rise}}$  approximately controls the amount of time the SFR is rising at early times; we set this parameter equal to 2 Gyr at all radii as in [Johnson et al. \(2021\)](#). Our e-folding timescales of  $\tau_{\text{sfr}}$  are taken from a fit to this functional form to the  $\Sigma_{\star}$ -age relation in bins of  $R/R_e$  for  $10^{10.5} - 10^{11} M_{\odot}$  Sa/Sb Hubble type spiral galaxies reported by [Sánchez \(2020\)](#). The resulting values of  $\tau_{\text{sfr}}$  are long:  $\sim 15$  Gyr at the solar circle ( $R_{\text{gal}} = 8$  kpc) and as high as  $\sim 40$  Gyr in the outer disc (see Fig. 3 of [Johnson et al. 2021](#)). This is a consequence of flat nature of the  $\Sigma_{\star}$ -age relation reported by [Sánchez \(2020\)](#).

Within each  $\delta R_{\text{gal}} = 100$  pc ring, the normalization of the SFH is set by the total stellar mass of the Milky Way disc and the present-day surface density gradient assuming it is unaffected by stellar migration (see Appendix B of [Johnson et al. 2021](#)). For the former, we neglect



the contribution from the bulge and adopt the total disc stellar mass of  $5.17 \times 10^{10} M_{\odot}$  from [Licquia & Newman \(2015\)](#). For the latter, we adopt a double exponential form describing the thin- and thick-disc components. We take the scale radii of the thin- and thick-discs to be  $R_t = 2.5$  kpc and  $R_T = 2.0$  kpc, respectively, with a surface density ratio at  $R_{\text{gal}} = 0$  of  $\Sigma_t/\Sigma_T = 0.27$  based on the findings of [Bland-Hawthorn & Gerhard \(2016\)](#).

The [Johnson et al. \(2021\)](#) models run VICE in star formation mode, meaning that the user specifies the SFH and the amount of gas and infall at each timestep are calculated automatically by the code. Determining the gas supply requires an assumption about the star formation law (often referred to as “star formation efficiency” in the chemical evolution literature, though this term often has other meanings in, e.g., the star formation and feedback community). GCE models have and often still do adopt a single power-law relating the surface density of gas  $\Sigma_{\text{gas}}$  to the surface density of star formation  $\dot{\Sigma}_{\star}$  based on the findings of [Kennicutt \(1998\)](#). Recent studies, however, have revealed that the star formation law on a galaxy-by-galaxy basis is much more nuanced ([de los Reyes & Kennicutt 2019](#); [Ellison et al. 2021](#); [Kennicutt & de los Reyes 2021](#)). Some of the uncertainty regarding its details can be tracked back to the ongoing debate about the CO-to-H<sub>2</sub> conversion factor ([Kennicutt & Evans 2012](#); [Liu, Gao & Greve 2015](#)). Based on a compilation of the [Bigiel et al. \(2010\)](#) and [Leroy et al. \(2013\)](#) data shown in comparison to the theoretically motivated star formation laws of [Krumholz et al. \(2018, see their Fig. 2\)](#), [Johnson et al. \(2021\)](#) take a three-component power-law as their star formation law with index given by:

$$N = \begin{cases} 1.0 & (\Sigma_{\text{gas}} \geq 2 \times 10^7 M_{\odot} \text{ kpc}^{-2}) \\ 3.6 & (5 \times 10^6 M_{\odot} \text{ kpc}^{-2} \leq \Sigma_{\text{gas}} \leq 2 \times 10^7 M_{\odot} \text{ kpc}^{-2}) \\ 1.7 & (\Sigma_{\text{gas}} \leq 5 \times 10^6 M_{\odot} \text{ kpc}^{-2}). \end{cases} \quad (5)$$

The normalization of the star formation law is then set by letting the SFE timescale  $\tau_{\star} \equiv \Sigma_{\text{gas}}/\dot{\Sigma}_{\star}$  be given by the value derived observationally for molecular gas at surface densities where  $N = 1$ . The value of  $\tau_{\star}$  for molecular gas at the present day is taken to be  $\tau_{\text{mol},0} = 2$  Gyr based on [Leroy et al. \(2008, 2013\)](#) with a  $t^{1/2}$  time-dependence based on the findings of [Tacconi et al. \(2018\)](#) studying the  $\Sigma_{\text{gas}} - \dot{\Sigma}_{\star}$  relation as a function of redshift.

Because of the yields adopted in the [Johnson et al. \(2021\)](#) models, considerable outflows are required in order to predict plausible abundances. [Weinberg et al. \(2017\)](#) demonstrate analytically that to first order the equilibrium abundance of some element in the gas phase is determined by its yield and the mass loading factor  $\eta = \dot{\Sigma}_{\text{out}}/\dot{\Sigma}_{\star}$  with a small correction for the SFH. [Johnson et al. \(2021\)](#) make use of this to select a scaling of  $\eta$  with  $R_{\text{gal}}$  such that the equilibrium abundance as a function of radius corresponds to a reasonable metallicity gradient within the Galaxy (see their Fig. 3 and discussion in their § 3.1). Nonetheless, one can lower all yields and  $\eta$  at all  $R_{\text{gal}}$  by similar factors, and with all other model parameters held fixed, GCE models in general make similar predictions. The absolute scale of nucleosynthetic yields is a topic of debate (see discussion in, e.g., [Griffith et al. 2021a](#)), and some authors argue that outflows do not significantly alter the chemical evolution of the Galaxy disc and neglect them entirely (e.g. [Spitoni et al. 2019, 2021](#)). We investigate the impact of simultaneous variations in our yields and the efficiency of outflows in our models in § 4.2 below.

## 4 RESULTS

### 4.1 Evolution of a Fiducial Model

Our fiducial model adopts, together with the SN yields of [Johnson et al. \(2021, see discussion in § 2.1\)](#),  $y_{\text{N}}^{\text{CC}} = 3.6 \times 10^{-4}$  and our linear AGB star yield model with  $\xi = 9 \times 10^{-4}$ . Although we presented this model in comparison to the C11+C15 yields with  $\xi = 3 \times 10^{-4}$  in § 2.2, we find that a renormalization of this model is necessary to reproduce the [N/O]-[O/H] relation as observed with the [Johnson et al. \(2021\)](#) GCE model. We discuss this point further in § 4.2. To demonstrate the impact of stellar migration on N enrichment rates, we make use of the “diffusion” migration model in this section (see discussion in § 3).

In the left panel of Fig. 5, we plot the evolution of N and O abundances in the gas phase at five different Galactocentric radii. At early times, [O/H] is low and [N/O] reflects the ratio of the CCSN yields ( $[\text{N/O}]_{\text{cc}} \approx -0.7$ ). Consequently, the tracks in each ring are similar. Once lower mass stars begin to evolve through an AGB phase, they enrich the interstellar medium (ISM) with N but negligible amounts of O, increasing [N/O]. At this point, the tracks in each ring separate from one another. This separation is a consequence of the metallicity gradient in [O/H] being established early in the Galaxy’s evolution. Being an element produced primarily by CCSNe on short delay times, O reaches an equilibrium abundances on timescales of a few Gyr ([Weinberg et al. 2017](#)). Each ring therefore achieves equilibrium in O soon after AGB stars begin producing N, after which [N/O] continues to increase at an approximately fixed [O/H]. The separation of these evolutionary tracks further suggests that the [N/O]-[O/H] relation arises not as an evolutionary sequence but as a superposition of endpoints. That is, the relation that would be derived observationally for this model taking the N and O abundances at the present day from all rings (shown by the dotted black line; see discussion below) does not reflect the N and O abundances of the Galaxy in the past. Similar arguments have been made regarding low  $[\alpha/\text{Fe}]$  disc stars (e.g. [Schönrich & Binney 2009](#); [Sharma et al. 2021](#)).

Because there is a delay between a stellar population’s formation and N production from its AGB stars ( $\sim 250$  Myr in this model; see Fig. 4), stellar migration can in principle occur within this time interval. Although the bulk of migration occurs on longer timescales, this characteristic delay is comparable to the dynamical time of the Milky Way and is thus adequate for kinematic heating to at least begin. As a consequence, there may be a slight deficit or surplus of N-producing AGB stars in a given ring at some time induced by stellar migration. These tracks can thus move vertically in this plane in response to AGB stars moving between rings as the Galaxy evolves, entirely independent of the SFH and the nucleosynthetic yields of stars than formed at a given radius and time. We demonstrate this effect by comparing the solid blue and purple lines to their dotted counterparts, which denote the tracks when we neglect the impact of stellar migration on enrichment rates (i.e. the “post-processing” model from [Johnson et al. 2021](#)).

In the right panel of Fig. 5, we plot the gas-phase [N/O]-[O/H] relation predicted by the model at various snapshots. To obtain this, we simply take the N and O abundances in the ISM at a given output time for each  $\delta R_{\text{gal}} = 100$  pc ring at  $R_{\text{gal}} > 2$  kpc and plot them as a line. The relation is generally time-independent at  $T \gtrsim 5$  Gyr. Although there is some slight evolution toward higher [N/O], the total change in [N/O] over this time interval is well within the intrinsic scatter derived observationally (see Fig. 1). Even at  $T = 2$  Gyr at a redshift of  $z \approx 2.6$  (when the universe was 2.5 Gyr old as our model places the onset of star formation 500 Myr following the big bang;

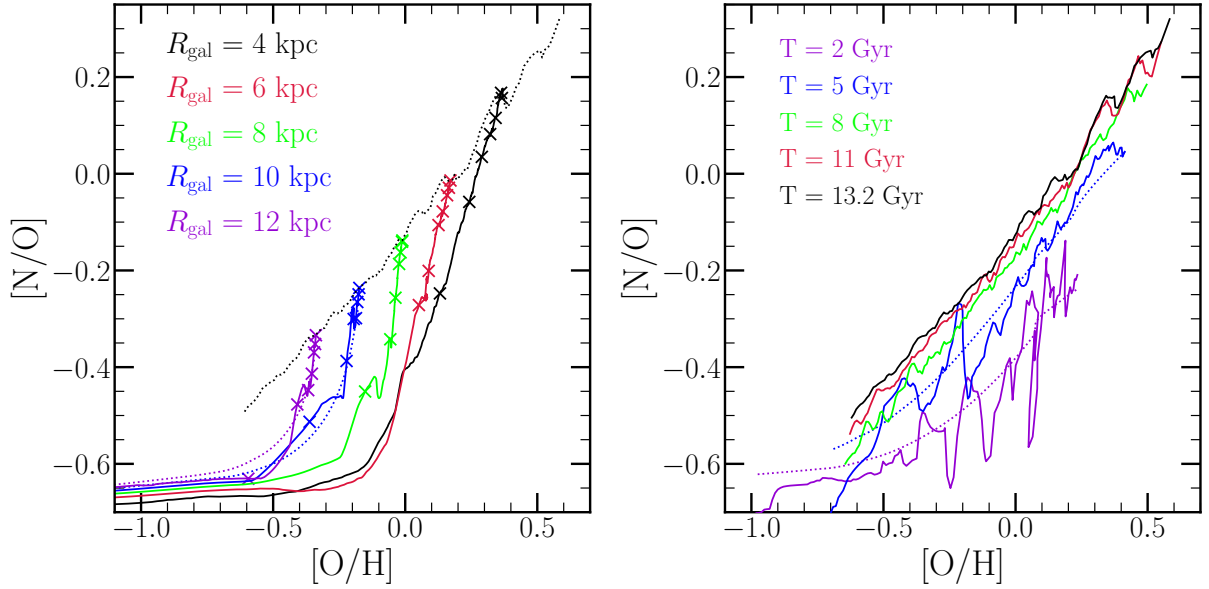


**Figure 5.** **Left:** The gas-phase  $[N/O]$ - $[O/H]$  relation parameterized by time at fixed radius (solid coloured lines) in the fiducial model. X's denote the abundances at  $T = 2, 4, 6, 8, 10, 12$ , and  $13.2$  Gyr (the present day) at all radii. The dotted black line is the same as the solid black line in the right panel. Coloured dotted lines mark the evolution of our model at  $R_{\text{gal}} = 10$  and  $12$  kpc when stellar migration is neglected (i.e. the “post-processing” migration model from [Johnson et al. 2021](#)). **Right:** The gas-phase  $[N/O]$ - $[O/H]$  relation parameterized by radius at various snapshots (solid coloured lines) in our fiducial model. Similar to the left panel, coloured dotted lines denote the resulting relation at  $T = 2$  and  $5$  Gyr when we neglect stellar migration.

see discussion in § 2.1 of [Johnson et al. 2021](#)),  $[N/O]$  at fixed  $[O/H]$  is only  $\sim 0.2$  dex lower than its value at the present day. Especially when considering the intrinsic scatter that would arise if we were to consider models with, e.g., different SFHs, this supports the notion that the  $[N/O]$ - $[O/H]$  relation has at most a weak dependence on redshift ([Vincenzo & Kobayashi 2018](#); [Hayden-Pawson et al. 2021](#)).

We again demonstrate the impact of stellar migration in the right panel of Fig. 6 by comparing the blue and purple solid lines to their dotted counterparts, which quantify the relation when we neglect stellar migration. This indicates that the complex features seen in the relation at all times are a consequence of migration as discussed above. The mechanism by which stellar migration imposes complex features in the  $[N/O]$ - $[O/H]$  plane is qualitatively similar to what [Johnson et al. \(2021\)](#) find for SN Ia production of Fe (see discussion in their §§ 3.1 and 3.4). They found that the SN Ia rate in this model can vary by as much as a factor of  $\sim 3$  at large radii ( $R_{\text{gal}} \gtrsim 9$  kpc). As a consequence, some of the resultant stellar populations are Fe-poor enough to present as young stars ( $\lesssim 6$  Gyr) with significantly super-solar  $[\alpha/\text{Fe}]$  ratios. Stars with these ages and chemical compositions have indeed been observed in the solar neighbourhood with APOGEE ([Chiappini et al. 2015](#); [Martig et al. 2015, 2016](#); [Warfield et al. 2021](#)). Although a substantial portion of these stars appear to have undergone mass transfer from a binary companion, making them appear younger than they truly are ([Jofré et al. 2016](#); [Yong et al. 2016](#); [Izzard et al. 2018](#); [Silva Aguirre et al. 2018](#); [Miglio et al. 2021](#)), some exhibit  $[C/N]$  ratios consistent with truly young ages ([Hekker & Johnson 2019](#)). [Johnson et al. \(2021\)](#) argue that the impact of stellar migration on enrichment rates is responsible for this intrinsically young sub-component. In the case of N, the effect is much smaller ( $\lesssim 0.1$  dex in  $[N/O]$ ), but Fig. 5 suggests there are some instances at early times where the effect is more substantial. This arises because our model predicts N yields to be ejected from stellar populations  $\sim 5$  times faster than Fe (even faster in our alternate yield models with larger contribution from high mass AGB stars; see Fig. 4 and dis-

cussion in § 2.3). Consequently, there is much less time for stellar migration to occur within the timescale of N production than there is within the timescale of Fe production. This underscores the argument from [Johnson et al. \(2021\)](#) that in order for nucleosynthetic yields to migrate significant distances along with their progenitor stellar populations, the timescale for production needs to be at least comparable to the migration timescale.

#### 4.2 Comparison to Observed Gas Phase Trends

We use the [Dopita et al. \(2016\)](#) measurements as our observational benchmark. They are a good representation of many results for gas phase N and O abundances (see Fig. 1), and they agree well with APOGEE stellar trends ([Vincenzo et al. 2021](#)). To make the comparison between different yield models more clear, we neglect the impact of stellar migration on enrichment rates and make use of the “post-processing” migration model in this section (see discussion in § 3).

In the left panel of Fig. 6, we compare the predictions of our multi-zone GCE model with each of the AGB star yield tables predicted from stellar evolution models (see Fig. 3 and discussion in § 2.2). Since it is based on the **C11+C15** yields, we find similar results with our linear model with a slope of  $\xi = 3 \times 10^{-4}$ . All four AGB star yield models fail to reproduce the gas-phase  $[N/O]$ - $[O/H]$  relation as observed. The **C11+C15** and **V13** yields are able to reproduce the qualitative trend, but with an incorrect normalization. The **K10** and **KL16+K18** yields, on the other hand, fail to reproduce the steadily sloped increase of  $[N/O]$  with  $[O/H]$ .

In order to successfully reproduce the observations, we find that we need to artificially amplify the **C11+C15** and **V13** yields by factors of  $\sim 3$  and  $\sim 2$ , respectively. Having originally compared our linear model to the **C11+C15** yields in Fig. 3 with a slope of  $\xi = 3 \times 10^{-4}$ , we amplify this value by a factor of 3 here as well. We illustrate the results of these modified yield models in the middle panel of Fig. 6.

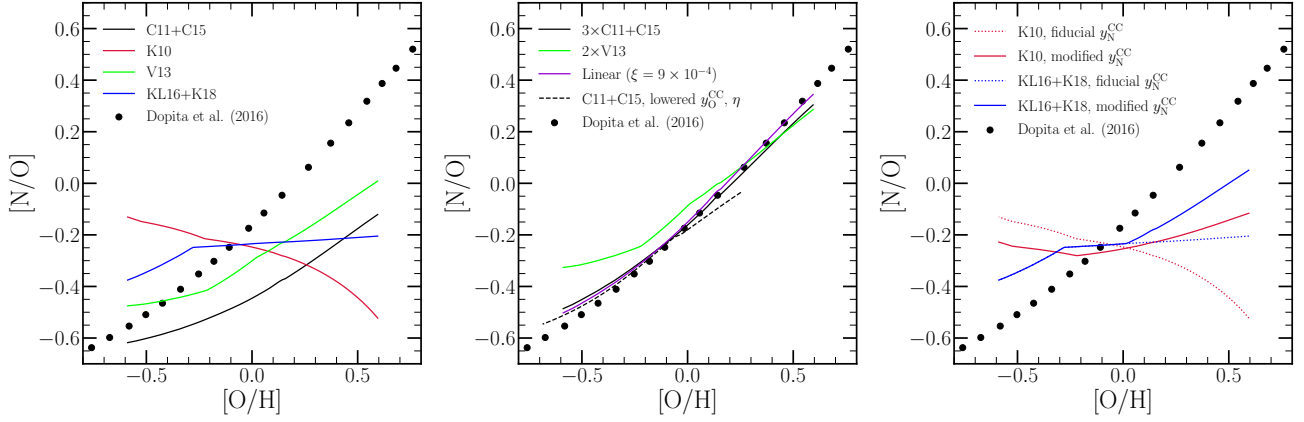


**Figure 6.** **Left:** The present-day gas-phase [N/O]-[O/H] relation predicted by our model with each of the four yield models based on stellar evolution models discussed in § 2.2, colour-coded according to the legend. We include the Dopita et al. (2016) measurements of this relation for local stars and HII regions (duplicated from Fig. 1) as the observational benchmark. **Middle:** The same as the left panel, but for a case where we artificially amplify the C11+C15 yields by a factor of 3 and the V13 yields by a factor of 2. We include our linear model as well, but with the slope amplified from  $\xi = 3 \times 10^{-4}$  as shown in Fig. 3 to  $\xi = 9 \times 10^{-4}$  since it is also based on the C11+C15 yields. **Right:** The same as the left panel, but comparing the predictions made by the K10 and KL16+K18 yields with our fiducial value of  $y_N^{\text{CC}}$  (dotted lines, same as left-hand panel) to those with alternate forms of  $y_N^{\text{CC}}$  (solid lines; see discussion in § 4.2). We show all predictions with “post-processing” migration model (see discussion in § 3).

Although the V13 model predicts an [N/O]-[O/H] relation that is slightly shallower than the Dopita et al. (2016) measurements, the predictions are reasonably within the scatter seen in Fig. 1. Rather than artificially amplifying the C11+C15 and V13 yields, we also find good agreement with the observed relation if we lower both our SN yields and our outflow mass loading factor  $\eta$  as a function of  $R_{\text{gal}}$  by similar factors from their values in Johnson et al. (2021). These parameters, which approximately determine the equilibrium abundance in a one-zone model (Weinberg et al. 2017), are tuned to reproduce a metallicity gradient in the disc that resembles that observed for the Milky Way (see discussion in § 2.4 of Johnson et al. 2021). However, since the yield and the outflow are simply source and sink terms in computing enrichment rates, the model makes similar predictions when both are lowered by the same factor. We demonstrate this point in the middle panel of Fig. 6 with the black dashed line for the C11+C15 model with both  $y_O^{\text{CC}}$  and  $\eta$  each lowered by a factor of 3. This model spans a different range in [O/H] because the relation between  $y_O^{\text{CC}}$ ,  $\eta$ , and the equilibrium abundance is only approximately one-to-one, but the predictions also exhibit good agreement with the Dopita et al. (2016) measurements.

Lowering our SN yields by a factor of 2 – 3 is plausible if a substantial fraction of massive stars collapse directly to black holes as opposed to exploding as SNe at the ends of their lives. Our IMF-averaged massive star yields (see discussion in § 2.1) are based on a Kroupa (2001) IMF combined with SN nucleosynthesis models in which most  $M > 8 M_{\odot}$  stars explode as a CCSN (e.g. Woosley & Weaver 1995; Chieffi & Limongi 2004, 2013; Limongi & Chieffi 2018; Nomoto et al. 2013), but recent results contest the validity of this assumption. The criteria for massive star explosions and which stars of what masses end their lives in “failed supernovae” has been a recent topic of interest from both theoretical (e.g. Pejcha & Thompson 2015; Sukhbold et al. 2016; Ertl et al. 2016) and observational perspectives (e.g. Gerke, Kochanek & Stanek 2015; Adams et al. 2017; Basinger et al. 2021). At present, no combination of a SN nucleosynthesis model with a physically motivated black hole landscape is able to reproduce the observed abundance patterns (Griffith et al. 2021a). Despite this, black hole formation still lowers SN yields by simply not producing explosive nucleosynthetic products and is thus an al-

ternate explanation for the failure of our fiducial model to reproduce the observed [N/O]-[O/H] relation with the C11+C15 and V13 yield models. With VICE’s `vice.yields.ccsne.fractional` function, designed to calculate values of  $y_X^{\text{CC}}$  for various elements (see discussion in § 2.1 here and in § 4 of Griffith et al. 2021a), we indeed find a value of  $y_O^{\text{CC}} = 0.0056$  using the W18 explosion model from Sukhbold et al. (2016) compared to our fiducial value of  $y_O^{\text{CC}} = 0.015$ .

Alternatively, Vincenzo et al. (2016a) are able to reproduce the [N/O]-[O/H] relation in chemical evolution models with the V13 yields by implementing a differential wind in which outflows remove O but not N from the star forming gas reservoir. Because the enrichment rates are the same as in our models with lowered SN yields, we again find similar results if simply add a portion of the SN yields (both CCSN and SN Ia) to the outflow while still lowering  $\eta$  at all radii. If SNe are the sources of outflow-driving winds, such a scenario is suggested by recent observational (Chisholm, Tremonti & Leitherer 2018) and theoretical arguments (Christensen et al. 2018), and could also account for this difference in our fiducial model if AGB stars do not significantly contribute to driving outflows.

With the K10 and KL16+K18 models failing to reproduce the qualitative trend of [N/O] with [O/H], none of the variations discussed above in the context of the C11+C15 and V13 yields are able to reproduce the observed results. Each of these alternate parameterizations corresponds to a renormalization of the predicted [N/O]-[O/H] relation, and with inaccurate slopes, there is no factor by which the predicted [N/O] ratios predicted by either K10 or KL16+K18 can be amplified or diminished in order to accurately explain the data. However, in principle it is possible that a metallicity-dependent CCSN yield of N could make up the difference.

If the K10 yields are to reproduce the observations, the overall N abundance must decrease at low [O/H] and increase at high [O/H]. We therefore construct the following parameterization of  $y_N^{\text{CC}}$ :

$$y_N^{\text{CC}} = (3.6 \times 10^{-4}) \left( \frac{Z}{Z_{\odot}} \right), \quad (6)$$

where  $Z_{\odot}$  is the total metallicity of the sun, for which we take a value of  $Z = 0.014$  based on the findings of Asplund et al. (2009) and Asplund, Amarsi & Grevesse (2021). We illustrate this CCSN

yield model with the slanted black dotted line in the left hand panel of Fig. 2. While our fiducial value of  $y_N^{\text{CC}} = 3.6 \times 10^{-4}$  best describes the rotating CCSN progenitor models of Limongi & Chieffi (2018), this alternate parameterization follows the non-rotating models published in Limongi & Chieffi (2018), Sukhbold et al. (2016), Nomoto et al. (2013), and Woosley & Weaver (1995) while maintaining the same base-line value of  $3.6 \times 10^{-4}$  at solar metallicity. If the KL16+K18 yields are to reproduce the observations, then contrary to the predictions made with the K10 yields, the [N/O] ratio at low [O/H] is fine (albeit slightly high by  $\sim 0.2$  dex). Instead, only the N abundance at high [O/H] needs correcting. We therefore construct a second alternate form of  $y_N^{\text{CC}}$  by retaining the value of the fiducial yield at sub-solar metallicity but assuming the value of equation (6) at super-solar abundances:

$$y_N^{\text{CC}} = (3.6 \times 10^{-4}) \max\left(1, \frac{Z}{Z_\odot}\right). \quad (7)$$

We compare our GCE model predictions with these alternate CCSN yield parameterizations for the K10 and KL16+K18 AGB star yield models in the right-hand panel of Fig. 6. These metallicity-dependent CCSN yields are able to make up some of the difference, but both models still predict an [N/O]-[O/H] relation that is simply too shallow to explain the observations. The inverse dependence of [N/O] with [O/H] with our fiducial CCSN yield and the K10 AGB star yields can be understood by the interaction between TDU and HBB (see discussion in § 2.2). Both effects are stronger at low metallicity, and since all of the K10 stars experiencing HBB also experience TDU (see their Table 1), such a result is unsurprising. This is also true for the KL16+K18 yields, but that model predicts a relatively flat [N/O]-[O/H] relation owing to differences in the  $^{14}\text{N}$  yields as a consequence of updates model inputs regarding opacity and mass loss (see discussion in § 2.2). In principle, there are parameterizations of  $y_N^{\text{CC}}$  which could reproduce the [N/O]-[O/H] relation with the K10 and KL16+K18 yield models - whatever makes up the difference at a given [O/H] can be assumed to be the corresponding CCSN yield. Such assumptions, however, would be challenged by both the rotating and the non-rotating SN nucleosynthesis models illustrated in Fig. 2. Despite these results, we cannot say with any confidence whether or not such a wide mass range of stars should experience both TDU and HBB during the AGB phase as in K10 and KL16+K18. Although this makes it difficult for these models to predict a monotonic increase of [N/O] with [O/H], there are many uncertain parameters required to predict yields from stellar evolution models, and we have only investigated a few of them here.

In short, we find that in order to reproduce the gas-phase [N/O]-[O/H] relation as observed, our model requires the sum total N yields from both CCSNe and AGB stars to scale roughly linearly with metallicity. Assuming our fiducial value of  $y_N^{\text{CC}} = 3.6 \times 10^{-4}$ , we previously illustrated this dependence in the right panel of Fig. 4. With the C11+C15 and V13 models specifically, our results suggest that these yields must increase by factors of 2 – 3 or that a similar fraction of massive stars must collapse directly to black holes; it may also be some mix of the two.

### 4.3 The Dependence of N Production on Age and Metallicity

Despite predicting a different mass dependence for  $y_N^{\text{AGB}}$  (see Fig. 3), the renormalized C11+C15 and V13 yield models both reproduce the slope of the [N/O]-[O/H] relation reasonably well. This is an indication that perhaps the metallicity dependence plays a much more important role than the delay time in establishing this correlation. To investigate this further, we consider two variants of our fiducial

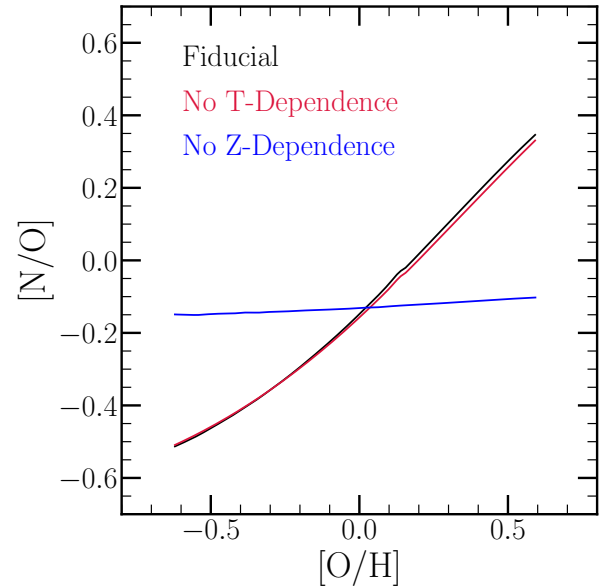


**Figure 7.** A comparison between our fiducial model with post-processing migration (black) and variations with the time dependence (red) and metallicity dependence removed (blue). To remove the time dependence, we pre-compute the AGB star yields of N from 13.2 Gyr old stellar populations as a function of metallicity as in the right panel of Fig. 4, then incorporate this into the prompt CCSN yields and set the delayed AGB star contribution to zero. To remove the metallicity dependence, we evaluate the yields at our assumed solar metallicity of  $Z = 0.014$  at all timesteps.

model: one with the dependence on stellar age removed from the enrichment rate calculations, and the other with the metallicity dependence removed. To make this comparison more straight-forward, we use the post-processing migration model (see discussion in § 3).

To remove the age dependence, we make use of VICE’s capability to let the user specify functional forms for nucleosynthetic yields. We pre-compute the N yields from all AGB stars associated with a 13.2 Gyr old stellar population as a function of progenitor metallicity in a similar fashion as in the right panel of Fig. 4. Since VICE works from IMF-averaged CCSN yields assumed to be injected instantaneously following a single stellar population’s formation (see discussion in § 2.1), we simply add this N yields to  $y_N^{\text{CC}}$  and set  $y_N^{\text{AGB}}$  to zero. In this model,  $y_N^{\text{CC}}$  inherits a metallicity dependence from the AGB star yields and has the exact shape as the curves in the right hand panel of Fig. 4. To remove the metallicity dependence, the procedure is much simpler: we simply evaluate  $y_N^{\text{AGB}}$  at our assumed solar metallicity of  $Z = 0.014$  at all timesteps. In this model, there is still a DTD to AGB star N production inherited from the stellar mass-lifetime relation and the mass dependence of the linear yield model.

We illustrate these model predictions in Fig. 7. The model with no age dependence is nearly identical to the [N/O]-[O/H] relation found in our fiducial model, while the model with no metallicity dependence is considerably different. This indicates that the metallicity dependence indeed plays a much larger role than the DTD in establishing the overall shape of the [N/O]-[O/H] relation. This is rather unsurprising given the short characteristic timescales of N production ( $\sim 250$  Myr, see the middle panel of Fig. 4). Mathematically, there is little difference in the enrichment rates if all of a stellar population’s N is produced immediately as opposed to from a sharply declining DTD. The metallicity dependence, however,



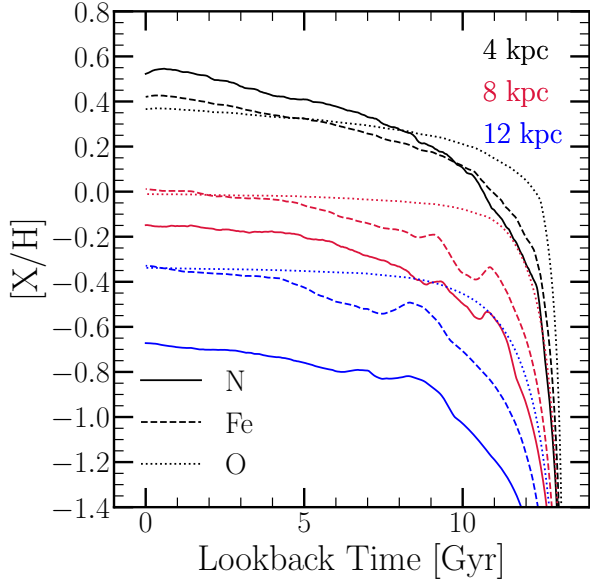


**Figure 8.**  $[N/H]$  (solid),  $[Fe/H]$  (dashed), and  $[O/H]$  (dotted) in the gas phase as a function of lookback time in the fiducial model at  $R_{\text{gal}} = 4$  (black), 8 (red), and 12 kpc (blue).

is paramount to the  $[N/O]$ - $[O/H]$  relation, which is expected given the results in Fig. 3 and consistent with previous arguments that the increase in  $[N/O]$  at high  $[O/H]$  is a consequence of secondary N production (Vila-Costas & Edmunds 1993; van Zee et al. 1998; Henry & Worthey 1999; Pérez-Montero & Contini 2009; Berg et al. 2012; Pilyugin et al. 2012; Andrews & Martini 2013; Hayden-Pawson et al. 2021).

We clarify that this characteristic timescale applies *only* to N and not to other elements produced in AGB stars. The DTD of AGB star enrichment is dictated by both the stellar mass-lifetime relation and the mass dependence of the yields from AGB stars. In general, various elements have a different mass dependence to their AGB star yield, and consequently, the associated DTD differs from element to element. N is somewhat unique in that its yields are dominated by high mass AGB stars, and generally these yields are at the expense of C and O isotopes consumed during HBB (Ventura et al. 2013). Other elements produced by the s-process often have the highest yields from lower mass AGB stars (e.g. strontium, for which the yields as reported by Cristallo et al. 2011, 2015 are dominated by  $M_{\text{ZAMS}} = 2 - 3 M_{\odot}$  progenitors; see Fig. 5 of Johnson & Weinberg 2020). The characteristic delay time of AGB star production will be as long as 10 Gyr if and only if the yields are dominated by  $\sim 1 M_{\odot}$  stars. Due to the steep nature of the mass-lifetime relation (Larson 1974; Maeder & Meynet 1989; Padovani & Matteucci 1993), elements whose yields are dominated by slightly more massive AGB stars will be produced on significantly shorter timescales (e.g.  $2 M_{\odot}$  stars live only  $\sim 1$  Gyr). Since the AGB star DTD should in principle differ from element to element, we caution against interpretations of AGB star nucleosynthesis which attribute a single characteristic delay time to this enrichment channel as that is likely only accurate for order of magnitude estimates and could lead to potentially spurious conclusions.

#### 4.4 Comparison to Stellar Abundances in the Milky Way Disc

In Fig. 8, we plot the evolution of N, O, and Fe abundances in the gas phase in the  $R_{\text{gal}} = 4, 8$ , and 12 kpc rings in our fiducial model with diffusion migration (see discussion in § 3).  $[N/H]$  is more correlated with  $[Fe/H]$  than  $[O/H]$  at all radii, and the relation persists up to lookback times of  $\sim 10$  Gyr. This arises in part because N and Fe are both produced in significant quantities by delayed enrichment sources while O is produced almost entirely on short timescales by CCSNe (see discussion in § 2). Although the production timescale of N from single stellar populations is short (see discussion in § 2.3), metallicity dependent yields require more abundance species such as O to be produced and reach an equilibrium before N yields stabilize. When many stellar populations are present, N abundances are somewhat limited in how fast they can increase due to the metallicity dependent nature of AGB star yields. Johnson & Weinberg (2020) found similar results regarding Fe and strontium; although strontium production timescales from single stellar populations are shorter than Fe, the bulk of the strontium production followed the bulk of the Fe production in one-zone models because of the metallicity dependence of the yields. As a consequence of both its slight delay and its metallicity-dependent yields, N reaches its equilibrium abundance on timescales similar to Fe rather than O (Weinberg et al. 2017). Because of its prompt enrichment source with metallicity-independent yields,  $[O/H]$  is nearly independent of lookback time as far back as  $\sim 10$  Gyr ago while  $[N/H]$  and  $[Fe/H]$  are not. This N-Fe correlation turns out to be important in understanding how these model predictions compare to stellar abundances as we discuss below.

Before comparing the predictions of GCE models to abundances derived from stellar spectra, it is essential to adjust the N abundances to account for internal processes known to alter the surface compositions of stars. After the CNO cycle has processed much of the C and O nuclei in a star's core into  $^{14}\text{N}$  during its main sequence lifetime, this N-rich material is mixed with the outer convective layers, increasing the N abundance in the photosphere. This effect is both predicted from theoretical models of stellar evolution and observed in open and globular clusters (Gilroy 1989; Korn et al. 2007; Lind et al. 2008; Souto et al. 2018, 2019). Since GCE models predict the birth abundances of stars, this effect must be taken into account.

Using MESA stellar evolution models (Paxton et al. 2011, 2013, 2015, 2018) with standard mixing prescriptions, Vincenzo et al. (2021) developed a prescription to approximate the birth abundances of C, N and O and apply it to a sample of APOGEE/Kepler red giants. They find good agreement between the APOGEE abundances and the Dopita et al. (2016) measurements, so our fiducial model's successful reproduction of the Dopita et al. (2016) trend is an indication that it also successfully reproduces the overall trend of  $[N/O]$  with  $[O/H]$  found for APOGEE disc stars. In this section, we focus on the stellar abundances, with which we can investigate trends with age and  $[O/Fe]$ .

Combining the Vincenzo et al. (2021)  $[N/O]$  ratios with the APOGEE stellar ages taken from Miglio et al. (2021), we illustrate the  $[N/O]$ -age relation in bins of  $[Fe/H]$  as predicted by our model in the left panel of Fig. 9. In good agreement with the observational measurements, the model predicts the  $[N/O]$ -age relation to be relatively flat in bins of  $[Fe/H]$ . This arises as a consequence of the N-Fe correlation and the fast approach to equilibrium in  $[O/H]$  as discussed above (see Fig. 8): a bin in  $[Fe/H]$  approximately corresponds to a bin in  $[N/H]$ , and with  $[O/H]$  more or less constant up to a lookback time of  $\sim 10$  Gyr, these bins in  $[Fe/H]$  also approximately correspond to bins in  $[N/O]$ . This is an important success of the model, because with uncorrected N abundances, Vincenzo et al. (2021) demonstrate

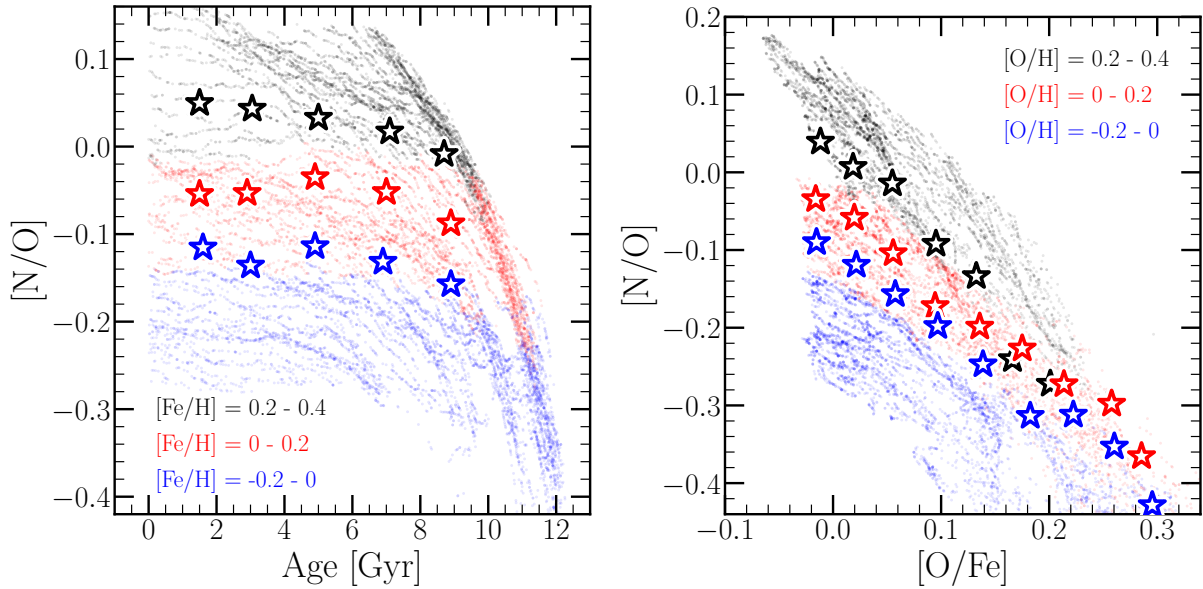


**Figure 9.** **Left:**  $[N/O]$  as a function of stellar age for 5000 stars randomly sampled from our model stellar populations in three bins of  $[Fe/H]$  (coloured points). Stars quantify the median trend in  $[N/O]$  with age using N abundances corrected for internal mixing processes reported by Vincenzo et al. (2021) in the same bins of  $[Fe/H]$ . **Right:** The same as the left panel, but instead showing  $[N/O]$  as a function of  $[O/Fe]$  in bins of  $[O/H]$ .

that the  $[N/O]$ -age relation exhibits a significant negative slope at fixed  $[Fe/H]$  (see their Fig. 7).

In the right panel of Fig. 9, we compare our model predictions to the  $[N/O]$ - $[O/Fe]$  relation reported by Vincenzo et al. (2021) at fixed  $[O/H]$ . The model correctly predicts a significant inverse relationship between  $[N/O]$  and  $[O/Fe]$ . This is again a consequence of the N-Fe correlation demonstrated in Fig. 8:  $[N/H]$  increases with  $[Fe/H]$ , so at fixed  $[O/H]$ ,  $[N/O]$  increases as  $[O/Fe]$  decreases. This is another important success of our model; Vincenzo et al. (2021) demonstrate that even when stellar N abundances are corrected for internal mixing processes, the chemical dichotomy in  $[N/O]$  between the high  $[\alpha/Fe]$  and low  $[\alpha/Fe]$  stars in the disc persists (for discussion of the Galaxy’s two distinct chemical populations see, e.g., Hayden et al. 2015; Weinberg et al. 2019, 2021; Griffith et al. 2021b). Although the Johnson et al. (2021) model does not reproduce this infamous  $\alpha$  bimodality in detail, a future iteration which does should also reproduce it for N based on these results.

Quantitatively, our model slightly overpredicts  $[N/O]$  in the lower metallicity bins in both panels of Fig. 9. In general, our model occupies a noticeably wider range in  $[N/O]$  than do the Vincenzo et al. (2021) measurements at all ages and all  $[O/Fe]$ . This could be a sign that the AGB star yields of N in our fiducial model scale slightly too strongly with the total metallicity  $Z$ . Since our fiducial model assumes an exactly linear scaling of the N yield with  $Z$ , this suggests that perhaps a slightly sub-linear scaling would be more accurate, but only barely because the discrepancies in Fig. 9 are at the  $\lesssim 0.1$  dex level.

#### 4.5 The Sources of Scatter in the $[N/O]$ - $[O/H]$ Relation

Schaefer et al. (2020) demonstrate that intrinsic scatter in the gas-phase  $[N/O]$ - $[O/H]$  relation is correlated with variations in the local SFE. This is expected from simple GCE models: with slower star formation, more AGB stars enrich the ISM by the time it reaches a given abundance, hence a higher  $[N/O]$  at a given  $[O/H]$  (e.g. Mollá et al. 2006; Vincenzo et al. 2016a). However, Schaefer et al. (2020)

do not rule out radial migration as another potential source of scatter in this relation. Our models, taking into account the effects of stellar migration on the enrichment rates while allowing full control over the SFH and the SFE through VICE, are the ideal tool with which to address this question.

To this end we construct two variants of our fiducial model, one in which the SFE exhibits 25% sinusoidal oscillations with time, and the other with the same 25% oscillations in the SFR. We modify the SFE timescale  $\tau_\star$  and the SFH  $\dot{\Sigma}_\star$  from the fiducial case in the following manner:

$$\tau_\star(R_{\text{gal}}, t) = \tau_{\star, J21}(R_{\text{gal}}, t) \left( 1 + 0.25 \sin\left(\frac{2\pi t}{2 \text{ Gyr}}\right) \right) \quad (8)$$

$$\dot{\Sigma}_\star(R_{\text{gal}}, t) = \dot{\Sigma}_{\star, J21}(R_{\text{gal}}, t) \left( 1 + 0.25 \sin\left(\frac{2\pi t}{2 \text{ Gyr}}\right) \right), \quad (9)$$

where  $\tau_{\star, J21}$  and  $\dot{\Sigma}_{\star, J21}$  refer to the SFE timescale and the SFH in the fiducial model taken from Johnson et al. (2021). In h277, the simulation from which the migration history of our model is drawn, we find that the overall SFE declines by a factor of  $\sim$  over the past  $\sim 9$  Gyr, an effect which is already built into  $\tau_{\star, J21}$ . Additionally, there are variations in the SFE at the  $\sim 25\%$  level between similar radii in the same snapshot as well as at fixed radii between successive snapshots. Based on this, an amplitude of 25% should capture typical variations seen in these quantities in hydrodynamical simulations. However, since h277 has a remarkably quiescent merger history (Zolotov et al. 2012), this may change in response to a major accretion event. **We can revise these few sentences with some observational references.**

In a real galaxy, variability in the SFE and the SFR is likely non-sinusoidal and not with constant amplitude. A sample of galaxies will have different amplitudes and be seen at different phases in their variability, and the impact of this on their N and O abundances will present as intrinsic scatter in the inferred trend. By comparing models with and without reasonable amounts of variability in these quantities while taking into account radial migration, we can nonetheless assess which quantities impact abundances more strongly and are

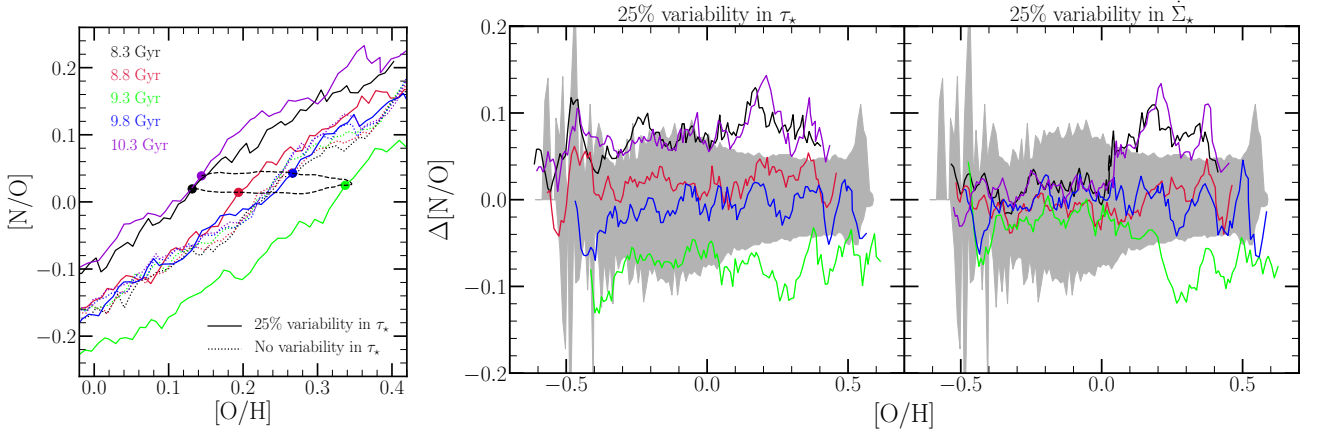


**Figure 10.** **Left:** One cycle of oscillations in the  $[N/O]$ - $[O/H]$  relation at high  $[O/H]$  induced by 25% sinusoidal variability in  $\tau_\star$  (solid coloured lines). Dotted lines show the  $[N/O]$ - $[O/H]$  relation at the same five snapshots in the fiducial model with no variability in  $\tau_\star$  but still with diffusion migration (see discussion in § 3). The black dashed line shows the time evolution the abundances at  $R_{\text{gal}} = 5$  kpc, with the times of each of the five snapshots marked by a coloured point. **Middle and Right:** For the same five snapshots in the left hand panel, the deviation in  $[N/O]$  at fixed  $[O/H]$  relative to the fiducial model for the case with 25% variability in  $\tau_\star$  (middle) and in  $\dot{\Sigma}_\star$  (right). The shaded regions in both panels quantify the width of the  $[N/O]$  distribution in  $10^{10.5} - 10^{11} M_\odot$  galaxies in MaNGA taken from Schaefer et al. (2020). In bins of  $[O/H]$ , we place the median  $[N/O]$  at  $\Delta[N/O] = 0$ , and the lower (upper) envelope denotes the 16th (84th) percentile of  $[N/O]$ .

thus the more likely causes of intrinsic scatter in the observed  $[N/O]$ - $[O/H]$  relation.

In the left panel of Fig. 10, we plot the predicted gas-phase  $[N/O]$ - $[O/H]$  relation at high  $[O/H]$  for five snapshots covering one cycle of fluctuations induced by variability in  $\tau_\star$  according to equation (8). This model predicts a  $\sim 0.15$  dex dynamic range in  $[N/O]$  at fixed  $[O/H]$ , whereas the fiducial model with no variability in  $\tau_\star$ , shown in the dotted lines, predicts the relation to be nearly constant over this time interval. While this suggests that stellar migration, present in both the fiducial model and these oscillatory variants, does not induce significant variability in the  $[N/O]$ - $[O/H]$  plane, we demonstrate below that the effects are nonetheless non-negligible. The minimal impact of stellar migration traces back to the timescales of N production from single stellar populations (see Fig. 4 and discussion in § 2.3): with most N production occurring within  $\sim 250$  Myr of a stellar population’s formation, most stars will not migrate far from their birth radius by the time they produce most of their N, and the resulting impact on abundances is small.

The behavior in the  $[N/O]$ - $[O/H]$  plane predicted by our variant with oscillatory SFE is driven by the constant tug-of-war between dilution and re-enrichment associated with oscillations in  $\tau_\star$ . In this model,  $\dot{\Sigma}_\star$  is the same as in Johnson et al. (2021), so it is not the SFR which varies but rather the gas supply. When the accretion rate increases, the ISM becomes diluted by gas at a primordial abundance, decreasing  $[O/H]$ . Because the AGB star yields of N in these models scale exactly linearly with metallicity  $Z$  (see discussion in § 2.2), the decrease in the N abundance due to the now lowered yields is in direct proportion to the amount of dilution, but with a slight delay. As a result,  $[N/O]$  is only marginally affected by the fluctuations in the overall abundance. The variations in the  $[N/O]$ - $[O/H]$  relation that the model predicts are much more of a consequence of variability in  $[O/H]$  than in  $[N/O]$ . We demonstrate this with the black dashed line in the left panel of Fig. 10, which traces the evolution of the abundances at  $R_{\text{gal}} = 5$  kpc over the same time interval. In general,  $[N/O]$  is affected only at the  $\sim 0.05$  dex level while  $[O/H]$  varies with an amplitude closer to  $\sim 0.25$  dex. As the gas supply falls off when  $\tau_\star$  decreases, enrichment proceeds in a gas-starved ISM, which increases  $[O/H]$  once more, but  $[N/O]$  to a lesser extent for similar

reasons, and the cycle repeats itself. We find similar results when we vary the SFH  $\dot{\Sigma}_\star$ . In this variant of our model,  $\Sigma_{\text{gas}}$  and consequently the abundances vary instead at a value of  $\tau_\star$  that varies only as much as the adopted  $\dot{\Sigma}_\star - \Sigma_{\text{gas}}$  relation from Johnson et al. (2021) dictates it should (see discussion in § 3).

In the middle and right panels of Fig. 10, we plot the scatter in the gas-phase  $[N/O]$ - $[O/H]$  relation inferred observationally by Schaefer et al. (2020). Using data from the MaNGA IFU survey (Bundy et al. 2015), they measure N and O abundances in 709,541 spaxels across 6,507 unique galaxies spanning  $10^9 - 10^{11} M_\odot$  in stellar mass. Since our model is appropriate for Milky Way mass galaxies, we focus our comparison on the  $M_\star = 10^{10.5} - 10^{11} M_\odot$  mass range (Licquia & Newman 2015), which cuts our sample sample to 197,787 individual N and O measurements from the MaNGA IFU spaxels. In narrow bins of  $[O/H]$ , we then compute the median  $[N/O]$  as well as the 16th and 84th percentiles of the  $[N/O]$  distribution. Placing the median  $[N/O]$  at  $\Delta[N/O] = 0$ , the shaded regions above and below 0 in Fig. 10 denote the difference between 16th and 84th percentiles of the distribution in each bin.

We then compare both of our oscillatory variants to the width of the  $[N/O]$  distribution by plotting the difference in  $[N/O]$  at fixed  $[O/H]$  between each variant and the fiducial model (i.e. the vertical offset between the solid and dotted lines in the left panel, and the equivalent thereof for the model with oscillations in  $\dot{\Sigma}_\star$ ). Both models produce offsets in  $[N/O]$  at fixed  $[O/H]$  which, as discussed above, are better characterized as offsets in  $[O/H]$  at an approximately fixed  $[N/O]$ , but the model with oscillations in  $\dot{\Sigma}_\star$  does not predict much of an effect at low  $[O/H]$ . This arises out of details in how we have parameterized these models (see discussion below). Fig. 10 suggests that our oscillatory models have an effect in the  $[N/O]$ - $[O/H]$  plane with an amplitude comparable to the width of the relation derived observationally by Schaefer et al. (2020). This is consistent with their argument that variations in the local SFE are the primary source of intrinsic scatter. However, our models suggest that the effects of stellar migration are still non-negligible. These effects are illustrated in the complex features on the curves in Fig. 10; without migration, they would be smooth and featureless as in Fig. 6 where we made use of the post-processing migration model. Fig. 10

suggests that an amplitude of  $\sim 0.05$  dex is not uncommon, as shown in Fig. 5 and discussed in § 4.1. With our oscillatory models inducing  $\Delta[\text{N/O}] \approx 0.1$  dex, migration is a smaller but nonetheless non-negligible effect.

The difference in predictions by our two oscillatory models at low  $[\text{O/H}]$  is a consequence of the mathematical form of  $\tau_{\star, \text{J21}}$  and the fact that we have specified our SFH a priori as opposed to the gas supply or the infall history. The low  $[\text{O/H}]$  end of the  $[\text{N/O}]-[\text{O/H}]$  relation arises at large  $R_{\text{gal}}$  due to the metallicity gradient. At these radii, our model predicts gas surface densities that are in the  $\dot{\Sigma}_{\star} \propto \Sigma_{\text{gas}}^{3.6}$  portion of our adopted  $\dot{\Sigma}_{\star} - \Sigma_{\text{gas}}$  relation (see equation 5 and discussion in § 3). However, since these models run from a specified SFH, it is not that the SFH is a strong function of the gas supply but rather that the gas supply is a weak function of the SFH. As a consequence, 25% oscillations in  $\dot{\Sigma}_{\star}$  have minimal impact on the ISM gas supply and thus the predicted abundances with how we have parameterized this model. At smaller  $R_{\text{gal}}$  (i.e. higher  $[\text{O/H}]$ ),  $\Sigma_{\text{gas}}$  varies more strongly with  $\dot{\Sigma}_{\star}$ , and as expected the impact on abundances is more substantial. If we were to adopt an alternate form of the  $\dot{\Sigma}_{\star} - \Sigma_{\text{gas}}$  relation, such as a purely linear or single power-law formalism as in many other GCE models (e.g. Spitoni et al. 2019, 2021; Grisoni et al. 2021), then this effect would be seen at all  $[\text{O/H}]$  when  $\dot{\Sigma}_{\star}$  oscillates. Alternatively, we expect similar results if we were to run an equivalent model through VICE where we specify the infall history a priori as it would allow more direct specification of the amount of dilution during each oscillation.

## 5 CONCLUSIONS

We have made use of the GCE models from Johnson et al. (2021) which characterize the Milky Way disc as a series of concentric rings with a uniform width  $\delta R_{\text{gal}} = 100$  pc. As in previous models with similar motivations (Matteucci & Francois 1989; Wyse & Silk 1989; Prantzos & Aubert 1995; Schönrich & Binney 2009; Minchev et al. 2013, 2014, 2017; Sharma et al. 2021), this model treats each individual ring as a conventional one-zone model of chemical evolution. The novel addition to this model, however, is that it takes into account the impact that radial migration has on enrichment rates by allowing stellar populations to enrich a distribution of radii as they migrate. We retained the IMF-averaged SN yields of O and Fe from Johnson et al. (2021), who in turn base these values off of Weinberg et al. (2017) and Johnson & Weinberg (2020). Assuming that the N yield from SNe Ia is negligible, we have investigated theoretical and empirical N yields from both massive stars and AGB stars.

If our fiducial CCSN yield of O is accurate ( $y_{\text{O}}^{\text{CC}} = 0.015$ ), then the CCSN yield of N required to produce the “plateau” of  $[\text{N/O}]_{\text{cc}} = -0.7$  at low  $[\text{O/H}]$  is  $y_{\text{N}}^{\text{CC}} = 3.6 \times 10^{-4}$ . Out of a handful of CCSN nucleosynthesis investigations (e.g. Woosley & Weaver 1995; Nomoto et al. 2013; Sukhbold et al. 2016), only Limongi & Chieffi (2018) present yields for rotating progenitors. With the non-rotating models falling short of this value (in some cases by multiple orders of magnitude; see Fig. 2), we argue that the effects of rotation are necessary to explain the N abundances seen at low  $[\text{O/H}]$ , consistent with recent results from Grisoni et al. (2021).

Various AGB star nucleosynthesis models predict vastly different yields of N as a function of progenitor mass and metallicity (see Fig. 3). Ascertaining the origin of these differences is difficult because each model folds in different assumptions regarding important evolutionary parameters such as mass loss, opacities of various isotopic species, convection and convective boundaries, and nuclear reaction networks (see discussion in, e.g., § 5 of Karakas & Lu-

garo 2016). Nonetheless the differences between yield models can be qualitatively understood by considering the differences between how TDU and HBB proceed in the stellar models (see discussion in § 2.2). In general, the most efficient N production occurs when both TDU and HBB occur simultaneously because each replenishment of C and O isotopes from the stellar core add new seed nuclei for HBB to process into  $^{14}\text{N}$  via the CNO cycle (Ventura et al. 2013). Different assumptions regarding mass loss and opacity can also impact the duration of a star’s AGB phase, inducing secondary effects on the N yields.

When weighted by the IMF (Kroupa 2001), the C11+C15 yields predict roughly equal contribution per interval in mass  $dM_{\star}$ . Each additional model shows a considerable contribution from AGB stars with ZAMS masses of  $\gtrsim 3 M_{\odot}$ . In all cases, the characteristic delay times for production by single stellar populations are on the order of a few hundred Myr. This is true even for the C11+C15 yields because the enrichment rates inevitably slow down due to the steep nature of the mass-lifetime relation; within a given time interval  $d\tau$ , the stellar mass range of AGB stars  $dM_{\star}$  quickly becomes narrow as  $\tau$  increases. This characteristic delay time only applies to N, however, which is somewhat unique in that its highest yields are from AGB stars of masses  $M_{\text{ZAMS}} \gtrsim 4 M_{\odot}$ . This is not necessarily the case for other elements with yields for lower mass AGB stars (e.g. strontium; see Fig. 4 of Johnson & Weinberg 2020 in comparison to Fig. 4 here for N). Nonetheless, the characteristic delay times for these elements will still be  $\lesssim 1$  Gyr unless their yields are dominated by  $\sim 1 M_{\odot}$  stars (a  $2 M_{\odot}$  star, for example, lives only 1 Gyr; Larson 1974; Maeder & Zahn 1998; Padovani & Matteucci 1993).

With a smooth SFH, we find that our model predicts the gas-phase  $[\text{N/O}]-[\text{O/H}]$  relation to be relatively time-independent up to lookback times of  $\sim 6 - 8$  Gyr. This is consistent with previous arguments that the relation is largely redshift-independent (Vincenzo & Kobayashi 2018; Hayden-Pawson et al. 2021). Similar to previous theoretical results regarding the low  $[\alpha/\text{Fe}]$  stars in the Milky Way disc (e.g. Schönrich & Binney 2009; Sharma et al. 2021; Johnson et al. 2021), we find that the  $[\text{N/O}]-[\text{O/H}]$  relation arises not out of an evolutionary sequence but as a superposition of endpoints. That is, the time evolution of each Galactic region through the  $[\text{N/O}]-[\text{O/H}]$  plane is not the same line as the  $[\text{N/O}]-[\text{O/H}]$  relation that would be observed at the present day in our model Galaxy (see Fig. 5).

Our fiducial model requires a renormalization of the AGB star yields of N in order to reproduce the  $[\text{N/O}]-[\text{O/H}]$  relation as observed. The C11+C15 and V13 yield models require an artificial amplification by factors of 2 and 3, respectively. However, these yield models are successful if we instead simultaneously lower our SN yields from Johnson et al. (2021) and the outflow mass loading factor  $\eta$  at all radii by similar factors (see Fig. 6). This is physically plausible if a substantial fraction of high mass stars collapse to black holes instead of ending their lives as CCSNe. Although there is presently no combination of a massive star nucleosynthesis model and a physically motivated black hole landscape able to reproduce the observed abundance patterns (Griffith et al. 2021a), extensive black hole formation still lowers SN yields by simply robbing the ejecta of the explosive nucleosynthesis component. This suggests that either N nucleosynthesis in AGB stars must be more efficient or that a substantial fraction of  $M \gtrsim 8 M_{\odot}$  stars must produce failed supernova; the answer may also be a combination of the two.

With both the K10 and KL16+K18 AGB star yield models, our model is unable to reproduce the monotonic increase of  $[\text{N/O}]$  with  $[\text{O/H}]$  as observed. This discrepancy persists if we consider alternate parameterization of the CCSN yield of



$N y_N^{CC}$  as suggested by the non-rotating models of Woosley & Weaver (1995), Nomoto et al. (2013), Sukhbold et al. (2016), and Limongi & Chieffi (2018). In general, we find that reproducing the  $[N/O]$ - $[O/H]$  relation requires total N yields from CCSNe and AGB stars to scale roughly linearly with the progenitor metallicity  $Z$ . We have the most success with a metallicity independent  $y_N^{CC}$  as suggested by CCSN models with rotating progenitors to set the zero-point and an AGB star yield of N which scales linearly with  $Z$  as in the right panel of Fig. 4. The normalization of the AGB star yields, however, depends on the SN yields and the efficiency of outflows as discussed above and in § 4.2.

To test our model against N abundances observed in stars, we make use of the measurements presented in Vincenzo et al. (2021). To estimate birth abundances of N, they use MESA stellar evolution models (Paxton et al. 2011, 2013, 2015, 2018) to correct the spectroscopically derived measurements for internal mixing processes known to affect the photospheric abundances of N in evolved stars (i.e. dredge-up of CNO cycle products; Gilroy 1989; Korn et al. 2007; Lind et al. 2008; Souto et al. 2018, 2019). They find that the  $[N/O]$  at fixed  $[Fe/H]$  is relatively age-independent, a result which our model successfully reproduces (see Fig. 9). This is a notable success of our model and the Vincenzo et al. (2021) estimates because with uncorrected N abundances,  $[N/O]$  at fixed  $[Fe/H]$  shows an inverse dependence on stellar age (see their Fig. 7). Additionally, our model predicts  $[N/O]$  to increase with decreasing  $[O/Fe]$ , a result which Vincenzo et al. (2021) derive for both corrected and uncorrected N measurements, suggesting that the chemical dichotomy between the thin and thick discs persists even when using birth abundances of N. Both of these results arise out of a correlation between  $[N/H]$  and  $[Fe/H]$  in the ISM predicted by the model. Although the characteristic delay time for N production from a single stellar population is only  $\sim 250$  Myr, metallicity dependent yields dictate that more abundant species like O must be produced in substantial amounts before N yields from AGB stars become significant. N production in a GCE model with many stellar populations is consequently more delayed than one might expect given the production timescales from only one; this is qualitatively similar to what Johnson & Weinberg (2020) find for strontium, another element with significantly metallicity-dependent yields from AGB stars. As a result, the model predicts  $[N/H]$  to correlate much more with  $[Fe/H]$  than  $[O/H]$  up to lookback times of  $\sim 10$  Gyr. This gives rise to both the flat nature of the  $[N/O]$ -age relation at fixed  $[Fe/H]$  and the inverse relationship between  $[N/O]$  and  $[O/Fe]$  (see Fig. 9 and discussion in § 4.4).

To investigate the sources of scatter in the  $[N/O]$ - $[O/H]$  relation, we construct two variations of the fiducial model from Johnson et al. (2021). In these alternate scenarios, we impose 25% sinusoidal oscillations on one of the SFE or the SFR as functions of time while incorporating the effects of stellar migration on the enrichment rates. **These oscillations are characteristic of what we see in h277, the galaxy from which our model's dynamical history is drawn (potentially swap this out for observational references).** In general, we find that these 25% oscillations induce variability in the gas-phase  $[N/O]$  ratio at fixed  $[O/H]$  that is a factor of  $\sim 2$  larger than that caused by stellar migration. This is a consequence of the quick production timescale of N by single stellar populations ( $\sim 250$  Myr, see Fig. 4 and discussion in § 2.3): there simply is not much time for orbits to dynamically evolve before most of a stellar population's N is ejected to the ISM. The change in  $[N/O]$  at fixed  $[O/H]$  caused by our oscillatory models is comparable to the scatter in the relation derived observationally by Schaefer et al. (2020) using data from the MaNGA IFU survey (Bundy et al. 2015). They demonstrate that this

scatter is correlated with variations in the local SFE, with lower SFE systems exhibiting higher  $[N/O]$  at fixed  $[O/H]$ . This is expected from simple GCE models, because with lower SFE, more AGB stars eject their N yields to the ISM by the time a given  $[O/H]$  is achieved (e.g. Mollá et al. 2006; Vincenzo et al. 2016a). Although they could not rule out migration as an additional source of scatter, this supports the argument by Schaefer et al. (2020) that local variations in the SFE is the primary driver, additionally suggesting that migration is a sub-dominant but still significant source.

The small impact of stellar migration on N enrichment rates is the opposite of what Johnson et al. (2021) find for SN Ia enrichment of Fe. Because the SN Ia DTD has a characteristic delay time closer to  $\sim 1$  Gyr and a significant tail to longer values, a substantial fraction of Fe production occurs on timescales similar to the migration timescale in this model. Consequently, the impact on enrichment rates is much stronger for Fe (as high as a factor of  $\sim 3$ ; see discussion in §§ 3.1 and 3.4 of Johnson et al. 2021). This is sufficiently strong such that it could explain the intrinsically young sub-component of the young  $\alpha$ -rich stars observed in the solar neighbourhood (Chiappini et al. 2015; Martig et al. 2015, 2016; Jofré et al. 2016; Yong et al. 2016; Izzard et al. 2018; Silva Aguirre et al. 2018; Warfield et al. 2021). Although our model suggests that the impact may be larger when the Galaxy was young, this effect is only at the  $\lesssim 0.5$  dex level for N (see Fig. 5 and discussion in § 4.1). This difference underscores the argument from Johnson et al. (2021) that in order for nucleosynthetic yields to migrate along with their progenitor stellar populations, the characteristic delay time for the enrichment of some element from a single stellar population must be at least comparable to the timescales of stellar migration.

The results outlined in this paper highlight the importance of empirically calibrated yields of all elements from all nucleosynthetic sources in GCE models. The combination of theoretically predicted yields with flexible computational tools such as VICE can provide powerful constraints for future models of stellar evolution and elemental production. When future spectroscopic surveys begin collecting data, studies such as this one will be essential to illuminating the lessons they have to teach us.

## 6 ACKNOWLEDGEMENTS

We are grateful to Amanda Karakas for valuable discussion on the physical processes affecting N production in asymptotic giant branch stars. We thank Paolo Ventura for providing asymptotic giant branch star yields at a wide variety of progenitor metallicities. We also thank Adam Schaefer for providing us a copy of the data from Schaefer et al. (2020). We acknowledge valuable discussion with Jennifer Johnson, Adam Leroy, Grace Olivier, Amy Sardone, Jiayi Sun, Todd Thompson, and other members of The Ohio State Astronomy Gas, Galaxies, and Feedback group. This work was supported by National Science Foundation grant AST-1909841. D.H.W. is grateful for the hospitality of the Institute for Advanced Study and the support of the W.M. Keck Foundation and the Hendricks Foundation. F.V. acknowledges the support of a Fellowship from the Center for Cosmology and Astroparticle Physics at The Ohio State University.

## REFERENCES

- Adams S. M., Kochanek C. S., Gerke J. R., Stanek K. Z., Dai X., 2017, *MNRAS*, **468**, 4968
- Anders E., Grevesse N., 1989, *Geochimica Cosmochimica Acta*, **53**, 197
- Andrews B. H., Martini P., 2013, *ApJ*, **765**, 140

- Andrews B. H., Weinberg D. H., Schönrich R., Johnson J. A., 2017, *ApJ*, **835**, 224
- Asplund M., Grevesse N., Sauval A. J., 2005, in Barnes Thomas G. I., Bash F. N., eds, *Astronomical Society of the Pacific Conference Series Vol. 336, Cosmic Abundances as Records of Stellar Evolution and Nucleosynthesis*. p. 25
- Asplund M., Grevesse N., Sauval A. J., Scott P., 2009, *ARA&A*, **47**, 481
- Asplund M., Amarsi A. M., Grevesse N., 2021, *A&A*, **653**, A141
- Basinger C. M., Kochanek C. S., Adams S. M., Dai X., Stanek K. Z., 2021, *MNRAS*, **508**, 1156
- Belfiore F., et al., 2017, *MNRAS*, **469**, 151
- Berg D. A., et al., 2012, *ApJ*, **754**, 98
- Berg D. A., Skillman E. D., Croxall K. V., Pogge R. W., Moustakas J., Johnson-Groh M., 2015, *ApJ*, **806**, 16
- Berg D. A., Pogge R. W., Skillman E. D., Croxall K. V., Moustakas J., Rogers N. S. J., Sun J., 2020, *ApJ*, **893**, 96
- Bigiel F., Leroy A., Walter F., Blitz L., Brinks E., de Blok W. J. G., Madore B., 2010, *AJ*, **140**, 1194
- Bilitewski T., Schönrich R., 2012, *MNRAS*, **426**, 2266
- Bird J. C., Kazantzidis S., Weinberg D. H., 2012, *MNRAS*, **420**, 913
- Bird J. C., Kazantzidis S., Weinberg D. H., Guedes J., Callegari S., Mayer L., Madau P., 2013, *ApJ*, **773**, 43
- Bird J. C., Loebman S. R., Weinberg D. H., Brooks A. M., Quinn T. R., Christensen C. R., 2021, *MNRAS*, **503**, 1815
- Bland-Hawthorn J., Gerhard O., 2016, *ARA&A*, **54**, 529
- Bloecker T., 1995, *A&A*, **297**, 727
- Bovy J., Leung H. W., Hunt J. A. S., Mackereth J. T., García-Hernández D. A., Roman-Lopes A., 2019, *MNRAS*, **490**, 4740
- Brooks A. M., Zolotov A., 2014, *ApJ*, **786**, 87
- Brooks A. M., Papastergis E., Christensen C. R., Governato F., Stilp A., Quinn T. R., Wadsley J., 2017, *ApJ*, **850**, 97
- Bundy K., et al., 2015, *ApJ*, **798**, 7
- Chiappini C., et al., 2015, *A&A*, **576**, L12
- Chieffi A., Limongi M., 2004, *ApJ*, **608**, 405
- Chieffi A., Limongi M., 2013, *ApJ*, **764**, 21
- Chisholm J., Tremonti C., Leitherer C., 2018, *MNRAS*, **481**, 1690
- Christensen C., Quinn T., Governato F., Stilp A., Shen S., Wadsley J., 2012, *MNRAS*, **425**, 3058
- Christensen C. R., Brooks A. M., Fisher D. B., Governato F., McCleary J., Quinn T. R., Shen S., Wadsley J., 2014a, *MNRAS*, **440**, L51
- Christensen C. R., Governato F., Quinn T., Brooks A. M., Shen S., McCleary J., Fisher D. B., Wadsley J., 2014b, *MNRAS*, **440**, 2843
- Christensen C. R., Davé R., Governato F., Pontzen A., Brooks A., Munshi F., Quinn T., Wadsley J., 2016, *ApJ*, **824**, 57
- Christensen C. R., Davé R., Brooks A., Quinn T., Shen S., 2018, *ApJ*, **867**, 142
- Cristallo S., et al., 2011, *ApJS*, **197**, 17
- Cristallo S., Straniero O., Piersanti L., Gobrecht D., 2015, *ApJS*, **219**, 40
- de los Reyes M. A. C., Kennicutt Robert C. J., 2019, *ApJ*, **872**, 16
- Dopita M. A., Kewley L. J., Sutherland R. S., Nicholls D. C., 2016, *Ap&SS*, **361**, 61
- Ellison S. L., Lin L., Thorp M. D., Pan H.-A., Scudder J. M., Sánchez S. F., Bluck A. F. L., Maiolino R., 2021, *MNRAS*, **501**, 4777
- Ertl T., Janka H. T., Woosley S. E., Sukhbold T., Ugliano M., 2016, *ApJ*, **818**, 124
- Frankel N., Rix H.-W., Ting Y.-S., Ness M., Hogg D. W., 2018, *ApJ*, **865**, 96
- Frankel N., Sanders J., Rix H.-W., Ting Y.-S., Ness M., 2019, *ApJ*, **884**, 99
- Friskhnecht U., et al., 2016, *MNRAS*, **456**, 1803
- Gerke J. R., Kochanek C. S., Stanek K. Z., 2015, *MNRAS*, **450**, 3289
- Gilroy K. K., 1989, *ApJ*, **347**, 835
- Governato F., et al., 2012, *MNRAS*, **422**, 1231
- Grevesse N., Noels A., 1993, in Prantzos N., Vangioni-Flam E., Casse M., eds, *Origin and Evolution of the Elements*. pp 15–25
- Grevesse N., Sauval A. J., 1998, *Space Sci. Rev.*, **85**, 161
- Griffith E. J., Sukhbold T., Weinberg D. H., Johnson J. A., Johnson J. W., Vincenzo F., 2021a, arXiv e-prints, [p. arXiv:2103.09837](https://arxiv.org/abs/2103.09837)
- Griffith E. J., Weinberg D. H., Buder S., Johnson J. A., Johnson J. W., Vincenzo F., 2021b, arXiv e-prints, [p. arXiv:2110.06240](https://arxiv.org/abs/2110.06240)
- Grisoni V., Matteucci F., Romano D., 2021, *MNRAS*, **508**, 719
- Gronow S., Cote B., Lach F., Seitzzahl I. R., Collins C. E., Sim S. A., Roepke F. K., 2021a, arXiv e-prints, [p. arXiv:2103.14050](https://arxiv.org/abs/2103.14050)
- Gronow S., Collins C. E., Sim S. A., Röpke F. K., 2021b, *A&A*, **649**, A155
- Hayden-Pawson C., et al., 2021, arXiv e-prints, [p. arXiv:2110.00033](https://arxiv.org/abs/2110.00033)
- Hayden M. R., et al., 2015, *ApJ*, **808**, 132
- Heger A., Woosley S. E., 2010, *ApJ*, **724**, 341
- Hekker S., Johnson J. A., 2019, *MNRAS*, **487**, 4343
- Henry R. B. C., Worthey G., 1999, *PASP*, **111**, 919
- Henry R. B. C., Edmunds M. G., Köppen J., 2000, *ApJ*, **541**, 660
- Hurley J. R., Pols O. R., Tout C. A., 2000, *MNRAS*, **315**, 543
- Izotov Y. I., Thuan T. X., Guseva N. G., 2012, *A&A*, **546**, A122
- Izzard R. G., Preece H., Jofre P., Halabi G. M., Masseron T., Tout C. A., 2018, *MNRAS*, **473**, 2984
- James B. L., Koposov S., Stark D. P., Belokurov V., Pettini M., Olszewski E. W., 2015, *MNRAS*, **448**, 2687
- Jenkins A., 1992, *MNRAS*, **257**, 620
- Jenkins A., Binney J., 1990, *MNRAS*, **245**, 305
- Jofré P., et al., 2016, *A&A*, **595**, A60
- Johnson J. A., 2019, *Science*, **363**, 474
- Johnson J. W., Weinberg D. H., 2020, *MNRAS*, **498**, 1364
- Johnson J. W., et al., 2021, *MNRAS*, **508**, 4484
- Karakas A. I., 2010, *MNRAS*, **403**, 1413
- Karakas A. I., 2014, *MNRAS*, **445**, 347
- Karakas A. I., Lugaro M., 2016, *ApJ*, **825**, 26
- Karakas A. I., Lugaro M., Carlos M., Cseh B., Kamath D., García-Hernández D. A., 2018, *MNRAS*, **477**, 421
- Kennicutt Robert C. J., 1998, *ApJ*, **498**, 541
- Kennicutt R. C., Evans N. J., 2012, *ARA&A*, **50**, 531
- Kennicutt Robert C. J., de los Reyes M. A. C., 2021, *ApJ*, **908**, 61
- Kodama T., Arimoto N., 1997, *A&A*, **320**, 41
- Korn A. J., Grundahl F., Richard O., Mashonkina L., Barklem P. S., Collet R., Gustafsson B., Piskunov N., 2007, *ApJ*, **671**, 402
- Kroupa P., 2001, *MNRAS*, **322**, 231
- Krumholz M. R., Burkhardt B., Forbes J. C., Crocker R. M., 2018, *MNRAS*, **477**, 2716
- Lacey C. G., Fall S. M., 1985, *ApJ*, **290**, 154
- Lagarde N., Decressin T., Charbonnel C., Eggenberger P., Ekström S., Palacios A., 2012, *A&A*, **543**, A108
- Larson R. B., 1974, *MNRAS*, **166**, 585
- Law D. R., Majewski S. R., 2010, *ApJ*, **714**, 229
- Leroy A. K., Walter F., Brinks E., Bigiel F., de Blok W. J. G., Madore B., Thornley M. D., 2008, *AJ*, **136**, 2782
- Leroy A. K., et al., 2013, *AJ*, **146**, 19
- Licquia T. C., Newman J. A., 2015, *ApJ*, **806**, 96
- Limongi M., Chieffi A., 2018, *ApJS*, **237**, 13
- Lind K., Korn A. J., Barklem P. S., Grundahl F., 2008, *A&A*, **490**, 777
- Liu L., Gao Y., Greve T. R., 2015, *ApJ*, **805**, 31
- Lodders K., 2003, *ApJ*, **591**, 1220
- Lodders K., Palme H., Gail H. P., 2009, *Landolt Börnstein*, **4B**, 712
- Maeder A., Meynet G., 1989, *A&A*, **210**, 155
- Maeder A., Zahn J.-P., 1998, *A&A*, **334**, 1000
- Majewski S. R., et al., 2017, *AJ*, **154**, 94
- Marigo P., 2002, *A&A*, **387**, 507
- Martig M., et al., 2015, *MNRAS*, **451**, 2230
- Martig M., et al., 2016, *MNRAS*, **456**, 3655
- Matteucci F., Francois P., 1989, *MNRAS*, **239**, 885
- Miglio A., et al., 2021, *A&A*, **645**, A85
- Mihalas D., Binney J., 1981, *Galactic astronomy. Structure and kinematics*
- Minchev I., Famaey B., Combes F., Di Matteo P., Mouhcine M., Wozniak H., 2011, *A&A*, **527**, A147
- Minchev I., Chiappini C., Martig M., 2013, *A&A*, **558**, A9
- Minchev I., Chiappini C., Martig M., 2014, *A&A*, **572**, A92
- Minchev I., Steinmetz M., Chiappini C., Martig M., Anders F., Matijevic G., de Jong R. S., 2017, *ApJ*, **834**, 27
- Mollá M., Vilchez J. M., Gavilán M., Díaz A. I., 2006, *MNRAS*, **372**, 1069
- Munshi F., et al., 2013, *ApJ*, **766**, 56
- Nomoto K., Kobayashi C., Tominaga N., 2013, *ARA&A*, **51**, 457

Padovani P., Matteucci F., 1993, *ApJ*, **416**, 26

Paxton B., Bildsten L., Dotter A., Herwig F., Lesaffre P., Timmes F., 2011, *ApJS*, **192**, 3

Paxton B., et al., 2013, *ApJS*, **208**, 4

Paxton B., et al., 2015, *ApJS*, **220**, 15

Paxton B., et al., 2018, *ApJS*, **234**, 34

Pejcha O., Thompson T. A., 2015, *ApJ*, **801**, 90

Pérez-Montero E., Contini T., 2009, *MNRAS*, **398**, 949

Pilyugin L. S., Vílchez J. M., Thuan T. X., 2010, *ApJ*, **720**, 1738

Pilyugin L. S., Grebel E. K., Mattsson L., 2012, *MNRAS*, **424**, 2316

Prantzos N., Aubert O., 1995, *A&A*, **302**, 69

Rogers N. S. J., Skillman E. D., Pogge R. W., Berg D. A., Moustakas J., Croxall K. V., Sun J., 2021, *ApJ*, **915**, 21

Sánchez S. F., 2020, *ARA&A*, **58**, 99

Schaefer A. L., Tremonti C., Belfiore F., Pace Z., Bershadsky M. A., Andrews B. H., Drory N., 2020, *ApJ*, **890**, L3

Schönrich R., Binney J., 2009, *MNRAS*, **396**, 203

Sellwood J. A., Binney J. J., 2002, *MNRAS*, **336**, 785

Sharma S., Hayden M. R., Bland-Hawthorn J., 2021, *MNRAS*, **507**, 5882

Silva Aguirre V., et al., 2018, *MNRAS*, **475**, 5487

Skillman E. D., Berg D. A., Pogge R. W., Moustakas J., Rogers N. S. J., Croxall K. V., 2020, *ApJ*, **894**, 138

Souto D., et al., 2018, *ApJ*, **857**, 14

Souto D., et al., 2019, *ApJ*, **874**, 97

Spitoni E., Silva Aguirre V., Matteucci F., Calura F., Grisoni V., 2019, *A&A*, **623**, A60

Spitoni E., et al., 2021, *A&A*, **647**, A73

Sukhbold T., Ertl T., Woosley S. E., Brown J. M., Janka H. T., 2016, *ApJ*, **821**, 38

Suliga A. M., Shalgar S., Fuller G. M., 2020, arXiv e-prints, p. arXiv:2012.11620

Tacconi L. J., et al., 2018, *ApJ*, **853**, 179

van Zee L., Salzer J. J., Haynes M. P., 1998, *ApJ*, **497**, L1

Vassiliadis E., Wood P. R., 1993, *ApJ*, **413**, 641

Ventura P., Di Criscienzo M., Carini R., D’Antona F., 2013, *MNRAS*, **431**, 3642

Ventura P., di Criscienzo M., D’Antona F., Vesperini E., Tailo M., Dell’Aglì F., D’Ercole A., 2014, *MNRAS*, **437**, 3274

Ventura P., Karakas A., Dell’Aglì F., García-Hernández D. A., Guzman-Ramírez L., 2018, *MNRAS*, **475**, 2282

Ventura P., Dell’Aglì F., Lugaro M., Romano D., Tailo M., Yagüe A., 2020, *A&A*, **641**, A103

Vila-Costas M. B., Edmunds M. G., 1993, *MNRAS*, **265**, 199

Vincenzo F., Kobayashi C., 2018, *MNRAS*, **478**, 155

Vincenzo F., Kobayashi C., 2020, *MNRAS*, **496**, 80

Vincenzo F., Belfiore F., Maiolino R., Matteucci F., Ventura P., 2016a, *MNRAS*, **458**, 3466

Vincenzo F., Matteucci F., de Boer T. J. L., Cignoni M., Tosi M., 2016b, *MNRAS*, **460**, 2238

Vincenzo F., et al., 2021, arXiv e-prints, p. arXiv:2106.03912

Wadsley J. W., Stadel J., Quinn T., 2004, *New Astron.*, **9**, 137

Warfield J. T., et al., 2021, *AJ*, **161**, 100

Weinberg D. H., Andrews B. H., Freudenburg J., 2017, *ApJ*, **837**, 183

Weinberg D. H., et al., 2019, *ApJ*, **874**, 102

Weinberg D. H., et al., 2021, arXiv e-prints, p. arXiv:2108.08860

Woosley S. E., Weaver T. A., 1995, *ApJS*, **101**, 181

Wyse R. F. G., Silk J., 1989, *ApJ*, **339**, 700

Yong D., et al., 2016, *MNRAS*, **459**, 487

Zahn J. P., 1992, *A&A*, **265**, 115

Zolotov A., et al., 2012, *ApJ*, **761**, 71

## Appendices

### A VICE

VICE<sup>1</sup> is an open-source PYTHON package designed to model chemical enrichment processes in galaxies with a generic, flexible model. With this paper, we mark the release of version 1.3.0 which presents a handful of new features:

(i) Users may select a mass-lifetime relation for stars from a list of several parameterized forms taken from the literature. Previously, only a single power-law was implemented, but this formulation underestimates lifetimes for stars with masses  $\gtrsim 4M_{\odot}$ ; now, the options include the equations presented in:

- Vincenzo et al. (2016b)
- Hurley, Pols & Tout (2000)
- Kodama & Arimoto (1997)
- Padovani & Matteucci (1993)
- Maeder & Meynet (1989)
- Larson (1974) (default)

Generally, chemical evolution models make similar predictions with each of these different forms of the mass-lifetime relation since their quantitative predictions are not considerably different from one another (see the section titled “Single Stellar Populations” under VICE’s science documentation for further discussion<sup>2</sup>). We select the Larson (1974) form as a default within VICE because it is typical compared to the others and requires the lowest amount of computational overhead (aside from the single power-law option).

(ii) We have added two additional tables of AGB star yields sampled at various progenitor masses and metallicities: the KL16+K18 and V13 models presented in this paper are new to VICE (see discussion in § 2.2 for details).

(iii) We have built in the SN Ia yields presented in Gronow et al. (2021b,a). These tables present yields for double detonations of sub-Chandrasekhar mass carbon-oxygen white dwarfs at various progenitor metallicities.

Although VICE includes built in SN and AGB star yield tables, users are not required to adopt any one of them for use in their chemical evolution models. Instead, it allows arbitrary functions of metallicity for both CCSN and SN Ia yields and functions of progenitor mass and metallicity for AGB star yields. It provides similar flexibility for additional parameters typically built into GCE models. VICE’s backend is implemented entirely in ANSI/ISO C, providing it with the powerful computing speeds of a compiled library while retaining such scientific flexibility within the easy-to-use framework of PYTHON.

Requiring a Unix kernel, VICE supports Mac and Linux operating systems; Windows users should install and use VICE entirely within the Windows Subsystem for Linux. On machines with x86\_64 hardware, it can be installed in a terminal via `pip install vice`. Users running ARM64 hardware (e.g. Macintosh computers with Apple’s new M1 processor) must install VICE by compiling from source, instructions for which can be found in the documentation. After installing, running `vice --docs` and `vice --tutorial` from a Unix terminal will launch a web browser to the documentation and to a

<sup>1</sup> Install (PyPI): <https://pypi.org/project/vice>  
Documentation: <https://vice-astro.readthedocs.io>  
Source Code: <https://github.com/giganano/VICE.git>

<sup>2</sup> [https://vice-astro.readthedocs.io/en/latest/science\\_documentation/](https://vice-astro.readthedocs.io/en/latest/science_documentation/)

jupyter notebook intended to familiarize first time users with VICE's API.